Nanostructured Metal Oxide Semiconductors towards Greenhouse Gas Detection

(Article begins on next page)

19 September 2024

Review

Nanostructured Metal Oxide Semiconductors towards Greenhouse Gas Detection

Mehran Dadkhah and Jean-Marc Tulliani *

Lince Laboratory, INSTM R.U, Department of Applied Science and Technology, Politecnico di Torino, Corso Duca Degli Abruzzi 24, 10129 Torino, Italy; mehran.dadkhah@polito.it
* Correspondence: jeanmarc.tulliani@polito.it

Abstract: Climate change and global warming are two huge current threats due to continuous anthropogenic emissions of greenhouse gases (GHGs) in the Earth's atmosphere. Accurate measurements and reliable quantifications of GHG emissions in air are thus of primary importance to the study of climate change and for taking mitigation actions. Therefore, the detection of GHGs should be the first step when trying to reduce their concentration in the environment. Throughout recent decades, nanostructured metal oxide semiconductors have been found to be reliable and accurate for the detection of many different toxic gases in air. Thus, the aim of this article is to present a comprehensive review of the development of various metal oxide semiconductors, as well as to discuss their strong and weak points for GHG detection.

Keywords: greenhouse gases; carbon dioxide; methane; nitrous oxide; fluorinated gases; metal oxides semiconductors; gas sensors

1. Introduction

Greenhouse gases (GHG) are compounds that absorb infrared radiation and prohibit it from radiating out into space and subsequently trap the heat in the atmosphere, contributing to global warming. Common GHGs are carbon dioxide (CO_2), methane (CH_4), nitrous oxide (N_2O) and fluorinated gases (F-gases: Hydrochlorofluorocarbons (HFCs), perfluorocarbons (PFCs), sulfur hexafluoride (SF_6) and nitrogen trifluoride (NF_3)). Figure 1 shows some activities responsible for greenhouse gas emissions into the atmosphere.
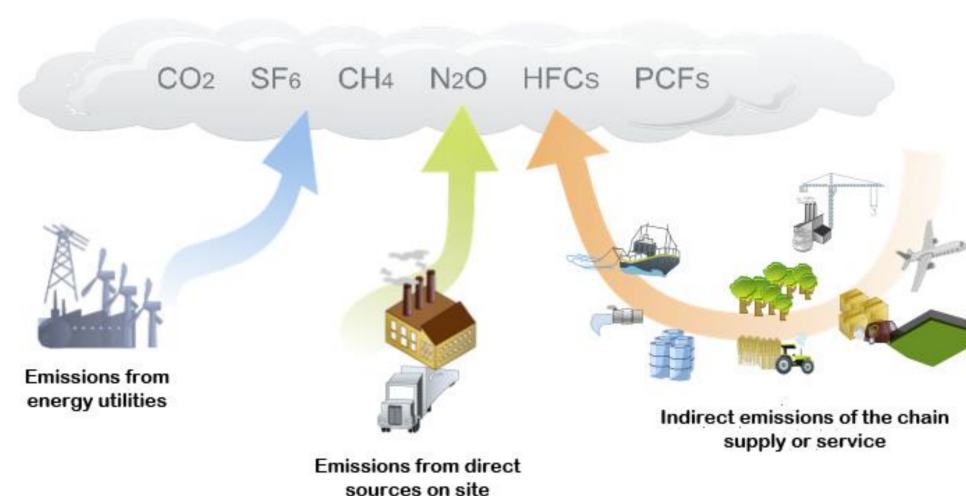

Figure 1. Sources of main greenhouse gas emission [1]; originally published under Creative Commons Attribution 3.0 Unported (CC BY 3.0) license.

The main reasons for the increment in CO_2 concentration in the atmosphere are fossil fuel and land-use change by about two-thirds and one-third, respectively [2]. During the first three decades about half of released CO_2 is removed, whereas a further 30% is removed over a few centuries and the remainder will stay in the atmosphere for many thousands of years [2].

Methane is the main component of natural gas which has been extensively utilized in domestic and industrial applications as a source of energy. It is emitted by both natural and anthropogenic sources with 40% and 60% proportions, respectively [3]. In comparison with carbon dioxide, CH_4 has more potential for global warming, so that any rapid increase in its concentration in the atmosphere would be devastating. Thus, at the recent COP26 (Conference of the Parties in Glasgow), over 100 countries signed up to the Global Methane Pledge to decrease global CH_4 emissions by 30% by 2030.

Agriculture, such as soil and management of animal manure, is the main anthropogenic source of N_2O. Moreover, it is naturally emitted from a broad range of biological sources that exist in soils and oceans. Nevertheless, the major contributions of N_2O are due to fossil fuel combustion, sewage treatment and chemical industrial productions such as nylon [4]. Nitrous oxide has a noticeable effect on climate change, global warming and stratospheric ozone layer depletion. In comparison with carbon dioxide, N_2O causes about 300 times atmosphere warming per unit weight, and it can remain in the atmosphere for up to about 114 years [2,5].

Fluorinated gases are synthetic gases used in industrial applications (as substitutes for ozone-depleting substances such as chlorofluorocarbons (CFCs), hydrochlorofluorocarbons (HCFCs), and halons) since they are not harmful to the atmospheric ozone because they do not damage the atmospheric ozone layer. Hydrofluorocarbons (HFCs) are, for example, extensively applied in industrial and commercial refrigeration systems, heat pump equipment and air conditioners. In addition, HFC gases are used as blowing agents for fire extinguishers, solvents, foams and aerosol propellants. Perfluorocarbons (PFCs) find many applications such as cosmetics, as well as in the pharmaceutical, refrigeration and electronic industries. These gases are also by-products of the aluminum smelting process (like CF_4, carbon tetrafluoride, PFC-14, which is the most abundant perfluorocarbon in the atmosphere). They can be found in old fire protection systems too [6]. PFCs can also be used as chemical tracer molecules to monitor the movement of supercritical CO_2 for carbon capture and sequestration purposes. To this aim, usually, a sample of carbon-based sorbents is collected from either soil gas or the atmosphere and then analyzed in a laboratory [7]. C_2F_6 (perfluoroethane, PFC-116) is released predominantly during aluminum production and semiconductor manufacturing. Among the PFC group, C_3F_8 (perfluoropropane, PFC-218) is the least abundant and is released during the production of semiconductors and utilized as a refrigerant as well [8]. In comparison with CO_2 gas, F-gases such as SF_6 have a significant role in global warming (23,000 times more than CO_2). From a climate overview, hydrofluorocarbons are by far the most relevant fluorinated gases with a short atmospheric lifetime. In contrast, PFC gases, including CF_4, C_2F_6 and C_3F_8, are long lived and they can remain in the atmosphere for about 50,000, 10,000 and 2600 years, respectively.

One of the important GHGs is ozone that is formed and destroyed through the chemical reactions of other pollutants, including volatile organic compounds and NO_x [2,9]. Other chemically reactive gases such as sulfur dioxide and carbon monoxide with short atmospheric lifetime are commonly removed by raining or natural oxidation processes, so they have a variable concentration in the air

Table 1 presents some GHGs with their emission percentage in 2019 [10]. As can be seen, the highest and lowest emission percentage of greenhouse gases are attributed to carbon dioxide and CFC11, respectively.

Table 1. Contributions of the most important long-lived greenhouse gases to the increase in global radiative force from the pre-industrial era to 2019 [3].

Greenhouse Gases	Sources/Emission (%)
carbon dioxide	deforestation and combustion of fossil fuel/66
methane	wetlands, termites, ruminants, rice agriculture, fossil fuel exploitation, landfills and biomass burning/16
nitrous dioxide	soil and animal manure management, sewage treatment, fossil fuel combustion, and chemical industrial processes/7
CFC12 (dichlorodifluoro methane)	refrigeration systems/5
CFC11 (trichlorofluoro methane)	refrigeration systems/2
other	refrigeration systems, electrical insulator, semiconductors and LCD panels manufacturing, etc./4

As can be observed in Figure 2, in comparison to 2012, the global emissions of GHGs (excluding land-use change) increased to 52.4 gigatonnes of CO_2 equivalent (GtCO_2 eq) in 2019 with a rate of 1.1% per year. This was mainly due to the increase in CO_2 and CH_4 emissions to 0.9% and 1.3%, respectively. Methane and carbon dioxide have an approximate share of 19% and 73%, respectively, and are by far the most prominent greenhouse gases. In addition, in 2019, the emission of F-gases (3% share) and N_2O (6% share) have grown by a respective 3.8% and 0.8%. As can be obviously seen in Figure 2, in 2019, the total emission of GHGs (except those from land-use change) had 59% and 44% growth compared to 1990 and 2000, respectively. However, the reported emission growth in 2019 was equal to 1.1%, like the average annual growth rate between 2012 and 2019.

Global greenhouse gas emissions, per type of gas and source, including LULUCF
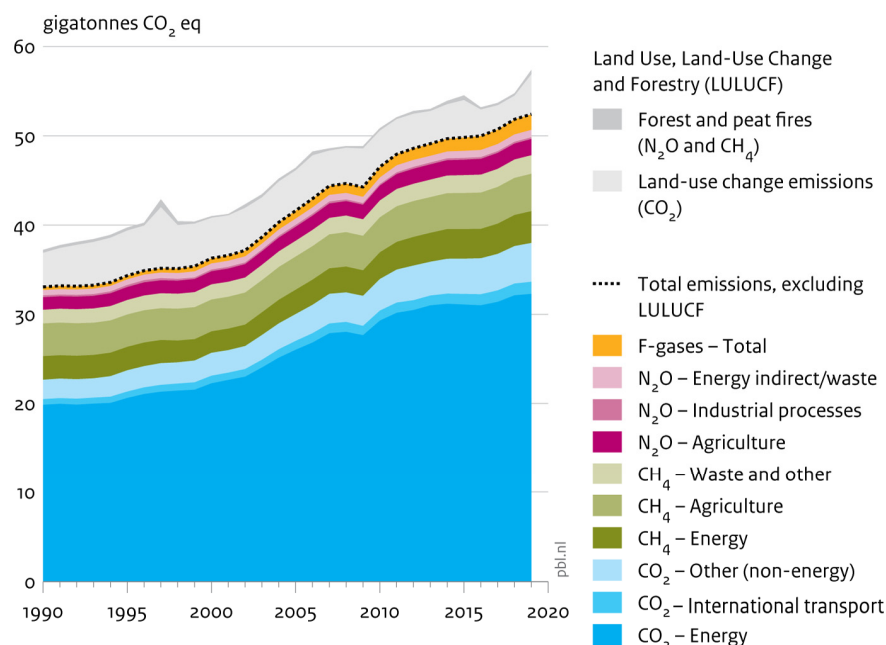
Source: CO_2, CH_4, N_2O excl. land-use change: EDGAR v5.0 FT2019; incl. savannah fires FAO; F-gas: EDGAR v4.2 FT2019
GHG from land-use change: CO_2 from Houghton & Nassikas 2017, CH_4 and N_2O from GFED4.1s 2020
Note: CO_2 eq with GWPs from IPCC AR4

Figure 2. Emissions of global greenhouse gases based on the type and source of gas. Reprinted with permission from reference [11].

The most significant effects of increasing concentration of greenhouse gases in the Earth's environment are the following [12,13]:

- Global warming,
- Intense droughts,
- Severe storms,
- Glaciers melting,
- Depletion of the ozone layer, which can occur by emission of CCl_4, CFCs and HCFCs,
- Changing the cycle of plant life and rain patterns,
- Rising sea levels and warmer oceans,
- Changing the lives of wildlife species.

For these reasons, already in 1997, the Kyoto Protocol tried to mitigate the emissions of the six main greenhouse gases, namely CO_2, N_2O, CH_4 and F-gases (HFCs, PFCs and SF_6). In 2015, the Paris Agreement was adopted because of the irreversible losses and damages caused to nature and society by climate change. Together with increasing pressure on natural resources and land area associated with the loss of species and ecosystems, climate change is a serious threat to the world's capacity to provide clean water, sufficient food and safe homes. Thus, the goal of the Paris Agreement was to limit the increase in the global average temperature to well below 2 °C (ideally 1.5 °C) above pre-industrial level. To achieve these long-term temperature targets, the parties agreed to reach their peaks of GHGs emissions as soon as possible and then to cut them drastically in the second half of the 21st century. Several countries, including the European Union (EU), have committed to be climate neutral by 2050 or later. These targets mean that a balance between anthropogenic releases and withdrawals by GHG sinks will have to be reached soon [14]. Despite the negative effect of GHGs, such as climate change, global warming, rise of ocean levels and environmental degradation, their presence in the atmosphere is vital to provide a habitable temperature. If the concentration of GHGs in the atmosphere becomes totally zero, the average surface temperature of the Earth would be about −18 °C [15].

In order to verify estimations of global emissions, it is essential to measure the concentration of GHGs in the air. To this aim, innovative, cheap, robust and accurate sensors are needed, and metal oxide (MOX)-based sensors have the potential to fulfil these requirements [13]. A gas sensor is a device for both qualitative and quantitative detection of the volatile substances in the vapor phase. In general, gas sensors are composed of a receptor and a transducer. A semiconductor gas sensor can be considered as a sensor including a semiconductor material which works as a receptor and/or transducer. Semiconductors are divided into two groups of oxides and non-oxides which are commonly based on silicon. Oxide semiconductors can be used as a receptor/transducer, while non-oxide ones cannot work as receptors because of the presence of an insulating layer [16].

Over the past few decades, most studies have focused on developing various types of sensors by applying different sensing materials and transduction stages [17]. In addition, an increasing number of papers investigated metal oxide semiconductor materials as gas sensors in environmental monitoring and in industrial applications due to their advantages such as low cost, easy synthesis methods, simplicity of use, fast recovery speed, non-toxicity, their abundance on earth, easy underlying mechanism, production of small devices, long lifetime and superior performance in detecting a wide range of target gases such as flammable and toxic gases. Of the many studied metal oxides, n-type oxides (like SnO_2, In_2O_3, WO_3, ZnO and γ-Fe_2O_3), as well as p-type oxides (like CuO and Co_3O_4) showed interesting gas sensing features. However, due to stability issues, when operating at high temperatures, only SnO_2, In_2O_3 and WO_3 have been adopted in commercial sensors [16].

The literature on MOX-based sensors has provided evidence that they have excellent sensitivity concerning many greenhouse gases (mainly, CO_2, CH_4, O_3 and N_2O) as well as a great response with the variation in the concentration of target gas and working temperature of the device. Nonetheless, MOX-based gas sensors need further improvement in their performances to accurately monitor greenhouse gases [18–20]. Hence, the aim of this paper is to overview the latest achievements (in the last decade) in the application of

nanostructured metal oxide semiconductor gas sensors for the detection of the main GHGs such as CO_2, CH_4, N_2O and fluorinated gases (F-gases).

2. Sensing Mechanism and Parameters of Gas Sensors

Chemoresistive sensors are generally made of a sensing film deposited on an electrically insulating layer (also called the substrate) provided with electrodes. This device can incorporate a heater, separated from the electrodes by the substrate [21]. The electrodes utilized for the readout of sensor resistance can be applied on one or two-electrode configurations. In a one-electrode configuration, a spiral heater based on noble metals (platinum, palladium and gold) is embedded inside the sintered ceramic bead, whereas in a two-electrode configuration, two electrodes are deposited on top or underneath the sensing material layer. As can be seen in Figure 3a, cylindrical type electrode is composed of a cylindrical alumina substrate with the electrode made of platinum deposited on it or a wire of Pt wound up around it. In this electrode, the sensing layer can be deposited on the platinum film or on the Al_2O_3 substrate. In disk type electrode (Figure 3b) the sensing material is in the form of a pellet with electrodes deposited on the two sides of the disk. The third electrode type is known as a parallel plate (Figure 3c), which has a planar substrate with a sensing layer. Then, two metal electrodes are deposited on both edges of the active film. Planar-type gas sensors consist of two electrodes that comb parallel to each other. This type of sensor can also be made of a sensing film that is deposited over inter-digitated electrodes (IDE s) as shown in Figure 3d [22].
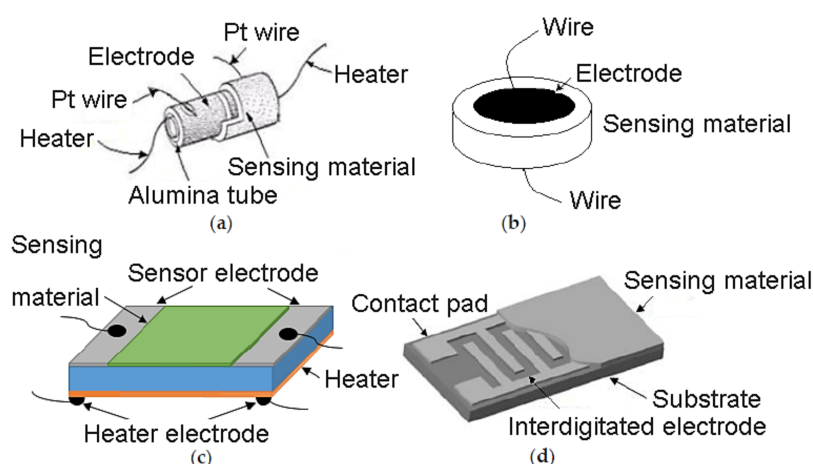

Figure 3. Various configurations of electrodes being used for chemiresistive gas sensors. (**a**) Cylindrical; (**b**) disk-type; (**c**) planar contacts; (**d**) inter-digitated electrode. Elaboration from reference [22]. Reprinted with permission under CC license.

In the case of metal oxide semiconductor sensors, the sensing mechanism is defined based on reduction-oxidation reactions between the target gas and the oxygen species, which are adsorbed on the surface of the sensing material. Details on sensing models can be found in several books and featured papers [21,23–27]. MOX sensors detect target gases due to reduction-oxidation reactions between the target gas and adsorbed oxygen species on their surface. When n-type metal oxide semiconductor sensors are exposed to a reducing gas atmosphere, like NH_3, they decrease the sensor's electric resistance. On the contrary, the adsorption process increases the surface resistance of the sensor in the presence of an oxidizing gas such as CO_2 and ozone. Due to their high electron affinity, oxygen species adsorb on the surface of n-type metal oxide semiconductors and trap free electrons. Electron trapping creates a potential barrier at the grain boundaries which limits the flow of electrons (i.e., there is the creation of a depletion layer or a space charge region). This leads to an increase of the MOX electric resistance. Successively, when the sensor is exposed to a reducing atmosphere, with gases such as NH_3, the gas molecules react with

active oxygen species and liberate free electrons in the bulk. This reduces the potential barrier height, favors the flow of electrons and reduces the sensor's electric resistance. In contrast, with oxidizing gases like CO_2 and ozone, the adsorption process raises the surface resistance [28]. In p-type metal oxide semiconductor sensors, electron exchanges in the presence of a gas cause a decrease or an increase in electron holes in the valence band when they are exposed to a reducing gas or an oxidizing gas, respectively [27].

The oxygen species on the surface of the MOX can be either physisorbed or chemisorbed in the function of the temperature. Below 150 °C, the molecular form dominates and O_2^- is physisorbed (Equation (1)), while above this temperature, the ionic species prevail: O^- below 250 °C and O^{2-} above 550 °C (Equations (2) and (3)) [21].

$$O_{2\,(ads)} + \acute{e} \rightarrow O_{2\,(ads)}^- \tag{1}$$

$$O_{2(ads)}^- + \acute{e} \rightarrow 2O^- \tag{2}$$

$$O_{2\,(ads)}^- + \acute{e} \rightarrow O_{(ads)}^{2-} \tag{3}$$

By adsorption of the oxygen molecules on the surface of MOX, the electrons transferred from the sensing material to these molecules. This movement leads to the production of negatively charged oxygen molecules on semiconductors in such a way that causes upward band bending at grain boundaries in the semiconductor (Figure 4).
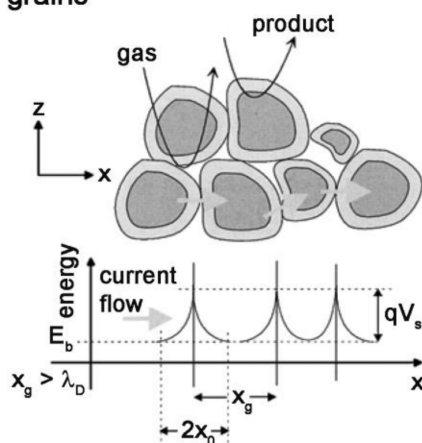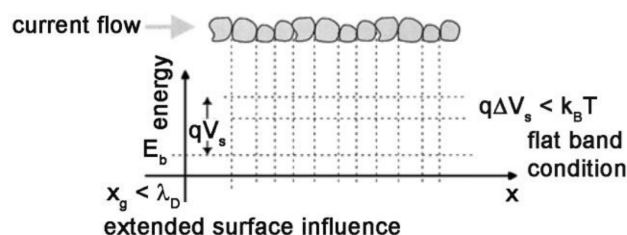
Figure 4. Schematic representation of a porous film with different grain size and energy band. (λ_D: Debye length; x_g: Grain size; x_0: Depletion layer thickness) Reprinted with permission from reference [21].

Figure 5 demonstrates the effective factors on the response of MOX gas sensors. To improve the sensor's performance, such as selectivity (the ability of a sensor to identify the target gas when in the presence of different gases; if the selectivity is low, the sensor response will be due to the contribution of any molecules in contact with it), sensitivity (the capacity to discriminate small changes in the analyte's concentration over a wide range of gas concentration values) and durability of the sensor, the crystallite size of MOX

should be as small as possible (in the nanometer range), as reported by Yamazoe [16]. Furthermore, sensitizers should be finely dispersed, and the thickness of sensing layers should also be optimized [29]. In fact, in large grains containing partly depleted layers, the conduction in the entire grain width is not affected by surface reactions. Thus, the process of conduction occurs in the bulk region more conductive compared to the outer space charge region. When the conduction is parallel to the surface, the sensor presents a limited sensitivity [21]. For thin layers, the thickness of the layer is comparable to λ_D (the Debye length, a measure of the electronic "crosstalk" between the surface phenomena and the bulk electronic properties [30]), the influence of surface processes is extended to the whole layer (there is no longer a conducting channel and a resistive one), and the conduction is then a function of the concentration of electrons influenced by the surface reactions.
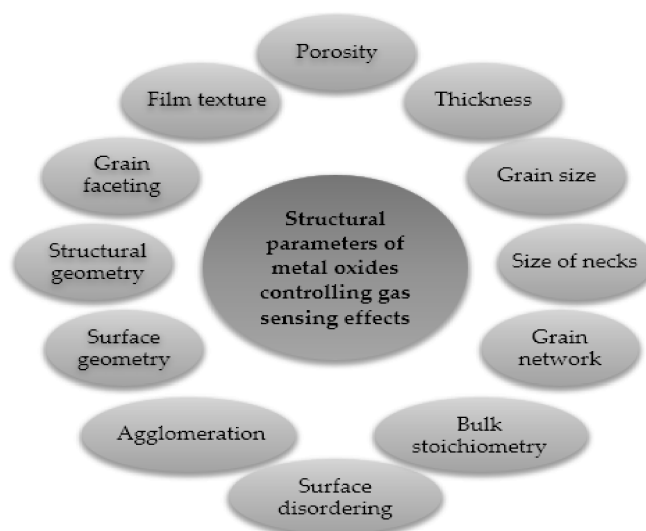

Figure 5. MOXs features that influence their gas-sensing properties. Elaboration from reference [31].

In the case of porous layers, there are three possibilities for the necks between grains, including surface/bulk, grain boundary and flat bands, which are for enough large necks, large grains not sintered together and small grains with small necks, respectively (Figure 4). Moreover, as can be seen in Figure 4, the barrier height (qVS) at the grain boundaries is a function of the density of surface state NS modulated by the previously mentioned oxidation-reduction reactions.

The performance of the sensor depends on various properties, including response and recovery time (the time needed for a sensor to reach a variation of 90% of the total resistance, impedance or capacitance during gas adsorption or desorption, respectively), selectivity, sensitivity, operating temperature (the temperature at which the gas sensor shows the highest response with respect to the target gas) and limit of detection (LOD, the minimum concentration of target gas detected at a known confidence level), etc. [13]. Furthermore, reversibility (the capacity of a sensor to recover its initial resistance, impedance or capacitance value when the atmosphere with the target gas is switched to fresh air), long-term stability, consumption of energy and low dependence on humidity are other significant parameters for gas [32]. Generally, pure metal oxide gas sensors have some disadvantages, including poor selectivity and low sensitivity towards lower concentration of target gas, high consumption of energy and high operating temperature [33].

Any method able to modify on MOX surface, surface stoichiometry (oxygen vacancies are responsible for enhanced performances), work function, the binding energy of atoms, the concentration of carbon contaminants, chemical activity of surface and so on is effective at improving gas sensor performances. However, to this aim, surface modification of metal oxides and semiconductors by catalytically active atoms remains the most used method.

An increase of sensitivity and fast surface reactions can occur in the presence of catalysts on the surface of metal oxides and semiconductors [31].

Experimental results on MOX gas sensors showed that the addition of dopants or impurities significantly improved metal oxide semiconductors' features (Figure 6). The addition of various additives (based on catalytically active metals, non-metals, alkaline earth metals, metalloids, etc.) to the MOX is one of the main techniques to increase the performance of gas sensors and this can be done by bulk doping and surface doping [30]. Table 2 shows some of these additives. In addition, it should be noted that the main doping additives include noble and transition metals [30].
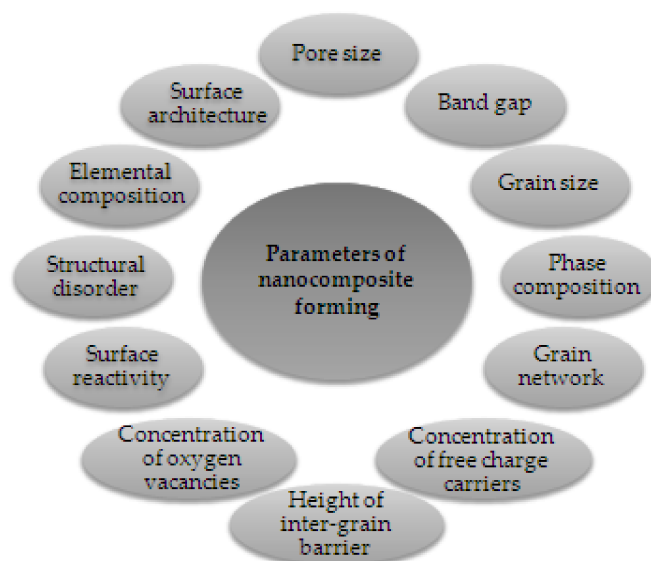

Figure 6. Features influenced by metal oxide–metal oxide nanocomposite formation. Elaboration from reference [34].

Table 2. Influence of bulk doping on gas-sensing characteristics of SnO_2 and In_2O_3 sensors [13].

Additive	Effect	Nature
Noble metals (less than 5 wt%) (Pd, Pt, Rh, Ag, Au)	increases response to reducing gases decreases operating temperature decreases response time	catalytic effect change of A/D parameters decrease of O_2 dissociation temperature
Al_2O_3, SiO_2	increases sensor response improves thermal stability	decrease of grain size decrease of area of intergrain contact increase of porosity
Ag (Ag_2O), Cu (Cu_2O)	increases response to H_2S, SO_2	two-phase system phase transformations during gas detection
Fe (Fe_2O_3)	increases response to alcohols	change of oxidation state
Ga (Ga_2O_3), Zn (ZnO)	increases sensor response	Decrease of grain size Increase of porosity
P, B	Improves selectivity	Creation of new phase
Ca, K, Rb, Mg	Increases sensor response Improves thermal stability	Decrease of grain size
La, Ba, Y, Ce	Improves thermal stability Increases sensor response	Stabilization of grain size (creation of new phase) Decrease of grain size
Transition MOXs (<0.5 wt%) (Co, Mn, Sr, Ni)	Increases sensor response Improves selectivity	Catalytic effect Change of electron concentration Change of A/D parameters Change of grain size

Humidity usually exhibits reducing features, even if the oxidizing effect of water was evidenced by Staerz et al. on the WO_3 surface at 300 °C [35]. However, when doping with precious metals, water dissociation is not favored on either metal's close-packed face, as Rh and Pt are relatively unreactive [36]. Calculations showed that neither H_2O bilayers, nor half-dissociated monolayers, are thermodynamically stable on clean Rh(111). On the contrary, impurities such as C atoms provide favorable binding sites for H atoms detached from H_2O molecules [37].

Nevertheless, it is almost impossible to synthesize polycrystalline metal oxide films with suitable grain faceting. In 1D sensors, planes and faceting depend on the synthesis parameters that allow a tighter control of the sensor's performances [31].

Many studies reported that the power consumption and operating temperature of MOX gas sensors have decreased by using nanocomposites and make them suitable for remote monitoring systems [38,39]. Moreover, the utilization of nanocomposites as sensing materials can remarkably improve the selectivity of sensors [40]. By solving the 3 "S" problems of gas sensors (the improvement of sensitivity, selectivity and stability) with metal oxide nanocomposites, these could be successfully applied for the detection of GHGs [34].

Sensor's resistance changes when in presence of the test gas. The response of n-type and p-type MOSs-base gas sensor can be defined by Equations (4) and (5), respectively:

$$S^n = \frac{R_g}{R_a} \tag{4}$$

$$S^p = \frac{R_a}{R_g} \tag{5}$$

In Equations (4) and (5), R_a shows the resistance of the gas sensor in the presence of reference gas that is usually air, and R_g is the gas sensor's resistance when target gas exists [32]. Table 3 shows the resistance changes in the presence or absence of oxidizing/reducing gases in the case of metal oxide semiconductor-based gas sensors. Generally, reducing gases like CO, CH_4, H_2S, H_2, SO_2, NH_3 and HCHO leads to a decrease or an increase of conductivity in p-type and n-type semiconductors, respectively. Whereas the opposite behavior is reported in the case of oxidizing gases such as N_2O, NO, NO_2, O_3, Cl_2 and CO_2 for both types of semiconductor sensors [41].

Table 3. Change of resistance value for MOX-based sensor in the presence of oxidizing/reducing gases.

Type of Sensitive Material	Target Gas/Variation of Resistance	Response
p-type	reducing/increases	$S^n = \frac{R_g}{R_a}$
	oxidizing/decreases	$S^p = \frac{R_a}{R_g}$
n-type	reducing/decreases	$S^p = \frac{R_a}{R_g}$
	oxidizing/increases	$S^n = \frac{R_g}{R_a}$

3. Nanostructured Metal Oxide Semiconductor (NMOS)-Based Greenhouse Gas Sensors

3.1. Sensing of Carbon Dioxide (CO_2)

Several studies deal with the detection and control of CO_2 emission owing to its significant effect on global warming. The global concentration of CO_2 in the atmosphere was determined from historical ice core studies and recent air monitoring sites from 1950 to 2021 (Figure 7) [42]. As can be seen, the level of CO_2 in the atmosphere was about 310 ppm in 1950 compared to about 416.7 ppm in December 2021 [43], measured at Mauna Loa Observatory in HI, USA. The mean annual absolute increase over the past 10 years was

2.4 ppm/y. This resulted in the evolution of CO_2 sensors for monitoring and controlling the levels of CO_2 in the atmosphere and indoor air quality [44,45].
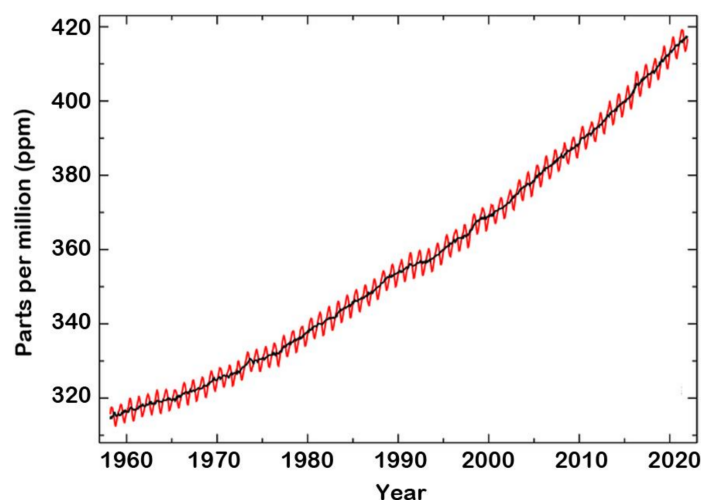

Figure 7. Global concentrations of CO_2 in the atmosphere during the period 1960–2021. Elaboration from reference [42]. © Global Monitoring Laboratory (GML) of the National Oceanic and Atmospheric Administration (NOAA).

Table 4 illustrates a summary of various metal oxide semiconductor-based CO_2 gas sensors. The ZnO nanorods of length (1–3 μm) without and with the addition of Ge, Nd and W were synthesized through the mechanochemical combustion method in reference [46]. In this paper, CO_2 sensors based on pure ZnO were less sensitive than the metal-doped ZnO ones under the air atmosphere. The authors justified these results based on the temperature that has a significant role in the adsorption of CO_2 molecules onto the surface of the ZnO based sensor and its electrical response. They determined the working temperature by measuring the sensitivity of all the doped ZnO samples under a constant concentration of CO_2 (1000 ppm). As can be seen in Figure 8, all ZnO specimens show similar behavior with regard to the effect of working temperature. In fact, the response of sensors increased with temperature and concentration of doping. Shohany et al. reported similar results with respect to the temperature [47].

Table 4. Brief summary of metal oxide semiconductor-based CO_2 gas sensors.

Material	Structure/Synthesis Method	Target Gas/ Concentration (ppm)	Operating T (°C)	Response (%)	Ref.
ZnO	thin film/chemical spray pyrolysis	CO_2/400	350	65	[48]
ZnO	nanowires/sol-gel	CO_2/15	200	1.04	[49]
ZnO	nanostructures films/sol-gel	CO_2/50 (sccm)	RT	1.0	[41]
Na/ZnO	spin-coated			81.9	
CeO$_2$	nano pellets/co-precipitation	CO_2/800	400	~33	[50]
Gd/CeO$_2$	nano pellets/co-precipitation	CO_2/800	250	45	
W/ZnO	nanorods/mechanochemical combustion	CO_2/1000	450	~98	[46]

Table 4. *Cont.*

Material	Structure/Synthesis Method	Target Gas/Concentration (ppm)	Operating T (°C)	Response (%)	Ref.
La/ZnO	nanopowders/hydrothermal	CO_2/5000	400	65	[51]
Ca/ZnO	nanopowders/sol-gel	CO_2/5%	450	113	[52]
Ca/ZnO	thin film/wet chemical	CO_2/25,000	400	32	[53]
$CuO/BaTiO_3$	$BaTiO_3$ spheroids decorated with CuO microleaves/co-precipitating	CO_2/1000	140	52	[54]
CuO	porous film/pneumatic spray pyrolysis	CO_2/100	RT	1.04	[55]
Zn/SnO_2	thin films/spray pyrolysis	CO_2/500	310	94.4	[56]
ZnO/SnO_2	nanocomposites/screen printing	CO_2/70	RT	~0.64	[57]
La_2O_3/SnO_2	nanofibers/electrospinning	CO_2/100	300	5.1	[58]
$Au-La_2O_3/SnO_2$	nanofibers/electrospinning, sputtering	CO_2/100	300	10.1	
La/SnO_2	nanofilm/hydrothermal, impregnation	CO_2/500	250	29.8	[59]
		CO_2/50		5.12	
CdO	nanowires/microwave-assisted wet chemical	CO_2/5000	250	~1.5	[60]
CdO	rod-like nanostructure/microwave radiation	CO_2/5%	250	3	[61]
Sn/CdO	spherical shaped structures/microwave assisted wet chemical			15	
CaO/In_2O_3	mesoporous/impregnation	CO_2/2000	230	~1.8	[62]
YPO_4	nanobelts/surfactant-assisted colloidal	CO_2/200	400	-	[63]
La_2O_3	microrods thin films/chemical bath deposition	CO_2/350	250	48	[64]
		CO_2/100		4.8	
$LaFeO_3/SnO_2$	nanocomposites porous film/sol-gel, hydrothermal	CO_2/4000	250	2.72	[65]
$LaFeO_3$	nanocrystalline/sol-gel	CO_2/2000	300	2.19	[66]
Pd/La_2O_3	thin-film/spray pyrolysis, ionic layer adsorption and reaction	CO_2/500	250	28	[67]
La_2O_3	thin-film/spray pyrolysis			13	
Cr/TiO_2	thin-film/RF magnetron sputtering	CO_2/10%	55	~9	[68]
Al_2O_3/TiO_2	heterostructure/ALD	CO_2/5	RT	30.6	[69]

RT = room temperature; ALD = atomic layer deposition.
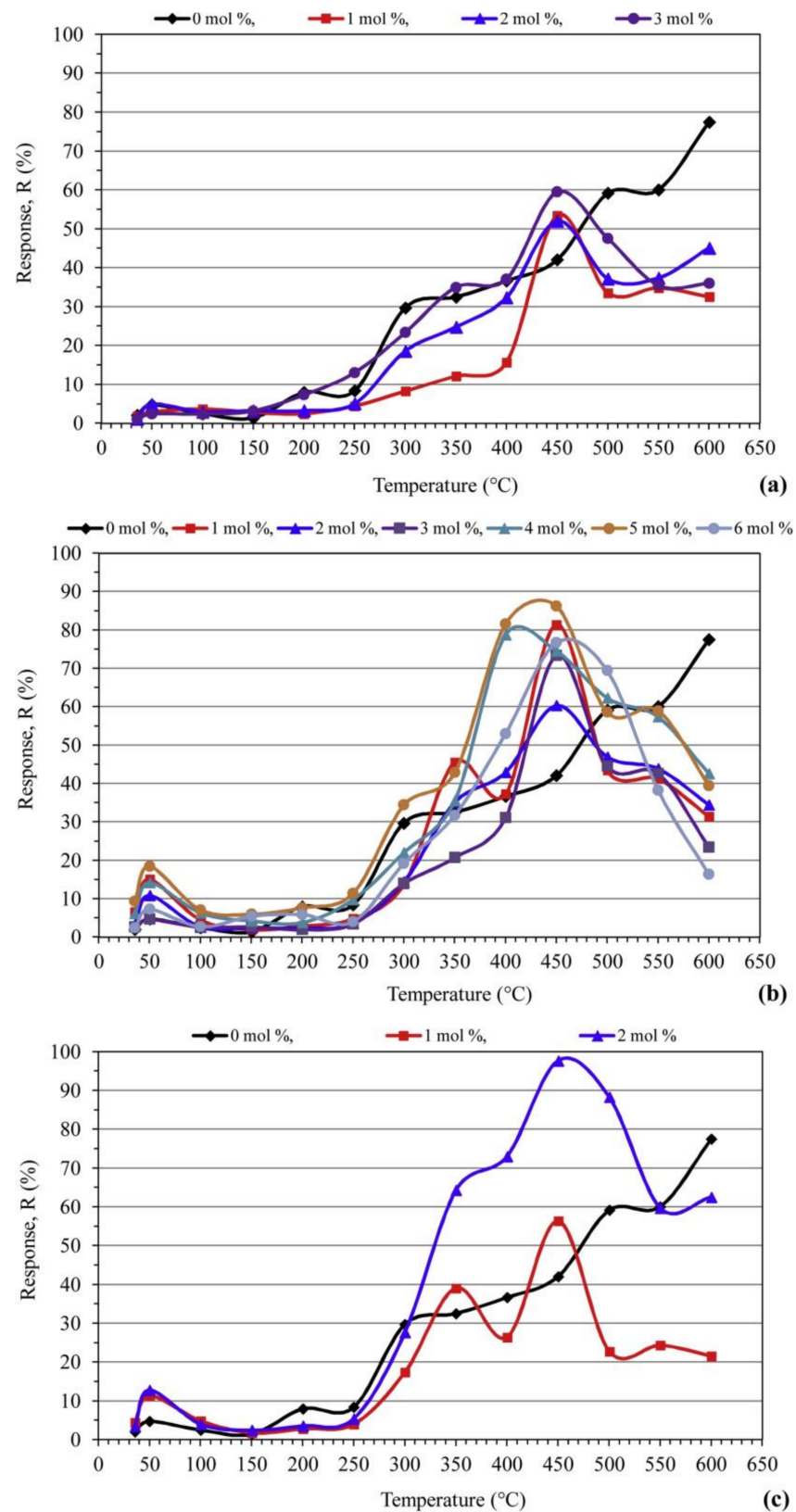
Figure 8. Variations of CO_2 sensor response with respect to temperature for ZnO nanorods based sensors: (**a**) Ge-doped; (**b**) Nd-doped; (**c**) W-doped. Reprinted with permission from reference [46].

From our experience on pure ZnO sensors for the detection of CO_2, this sensing material is very sensitive not only to carbon dioxide but also to water vapor. On ZnO

screen-printed sensors made from a commercial powder (Sigma Aldrich, Milan, Italy) and fired at 600 °C for 1 h, a sensor response was already observed from 100 ppm of CO_2 under dry air at 200 °C. However, the response was significantly affected when humidity (75% relative humidity at room temperature) was introduced (Figure 9b; 250 ppm of CO_2). A drift of the baseline was also evidenced during the measurements and in successive tests: The initial impedance value under dry air continuously increased (Figure 9a,b). To limit interferences with water vapor, an acetone gas sensor based on a core@shell structure ZnO nanowire-zeolite imidazole framework (ZIF) array was proposed by Yao et al. [70]. Both the selectivity and sensitivity to acetone were highly promoted due to the selectivity of zeolite imidazole frameworks which worked as sieve membranes. Subsequently, ZnO nanowires of various sizes were grown on a zinc oxide seeded sapphire substrate, followed by a hydrophobic and catalytic ZIF-CoZn coating. These authors found that thin ZnO (5 nm)-ZIF-CoZn nanowires had a better response toward 100 ppm acetone at 260 °C. In addition, the sensor response in the range from 10 to 90 RH% was almost constant. Such kinds of structures can also be investigated for the detection of GHGs in the air.
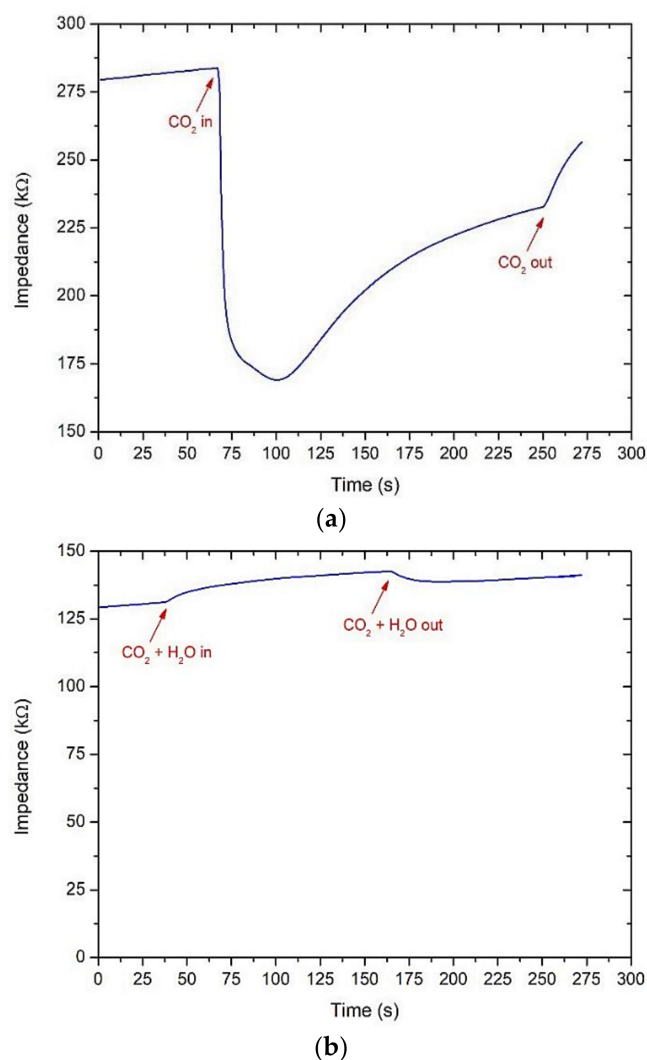

(a)

(b)

Figure 9. Change of the impedance value for a screen-printed ZnO sensor based on a commercial powder at 200 °C: under dry air (**a**); humid air (75 RH%) and 250 ppm of CO_2 (**b**).

Molybdenum and tungsten oxide nanostructured thin film-based gas sensors ($Mo_{1-x}W_xO_3$, x = in the range of 0.6–1) were produced by Mohamed A. Basyooni et al. through reactive RF magnetron co-sputtering at 400 °C to detect carbon dioxide at room temperature [71]. Their results showed fast responses from 6.53 to 12.25 s and recovery times from 0.06 to 4.02 s for the detection of CO_2 in the presence of UV light (365 nm) activation.

In recent years, there has been an increasing amount of literature on the synthesis of porous $LaFeO_3$-SnO_2 nanocomposites, Au-La_2O_3-doped SnO_2 nanofibers and $LaFeO_3$ microspheres by using various chemical methods in the presence of metals or metal oxides to increase the response of these sensors towards CO_2. Zhang et al. described the synthesis of the $LaFe_2O_3$/SnO_2 porous film-based sensor by mixing method and reported low response time (less than 20 s) at 250 °C [65]. The 5 wt% La_2O_3-SnO_2 nanofibrous was obtained by using the electrospinning process. The results showed significant improvement in the response towards many types of gases, particularly carbon dioxide [58]. Copper oxide has also attracted more attention as a sensing material for CO_2 detection with various structures such as nanocomposite, nanostructure, thick film and thin film [72–74]. Semiconducting pure and Gd doped CeO_2 nanostructure were prepared by co-precipitation method for detection of CO_2 in the range of 200–400 °C. According to the results, Gd-doped CeO_2 gas sensor showed maximum sensitivity at 250 °C, good stability and low operating temperature as well as a limit of detection of 800 ppm CO_2, while maximum response for pure CeO_2 was reported to be above 400 °C.

3.2. Sensing of Methane (CH_4)

Methane is the simplest hydrocarbon, explosive, odorless and colorless gas, but it is known as a highly flammable GHG. Moreover, it can be considered as a significant constituent of natural gas such as compressed natural gas (CNG) and liquified natural gas (LNG), which are used as fuel for vehicles as well as in the generation of heat and electricity production. According to the report of the World Meteorological Organization [75], the increase of CH_4 emissions from 2018 to 2019 (+11 ppb, part per billion) was negligibly lower than that reported between 2017 to 2018, although it was higher than the average during the last 10 years (+8 ppb/y). However, methane concentration in air is 262% higher with respect to the levels in 1750 when human activities started disrupting Earth's natural equilibrium. It reached 1889 ± 2 ppb in 2020. Thus, the detection of methane is essential due to the safety concern, although its detection is very difficult owing to the non-polarity and high enthalpy of the C-H bonds. Much of the current literature on MOX-based sensors pays particular attention to CH_4 detection [76].

Several authors have studied the use of various SnO_2 sensors for detecting CH_4. Pt-doped SnO_2 nanofibers (100–150 nm) were obtained by using the electrospinning method [77]. The results showed a response time of 4.48 s at 350 °C towards CH_4 in the presence of 20 mol% of Pt. Bunpang et al. [78] measured a response time of 3.9 s at 350 °C towards 1 vol% CH_4 for 0.5 wt% Cr-doped SnO_2 nanoparticles. In recent years, Lijia Yao et al. synthesized Pd-SnO_2 composite nanoporous structure by applying a low-power hydrothermal technique. They found that, in the presence of Pd, the gas sensing performance towards methane significantly increased compared to pure SnO_2. As shown in Figure 10, by addition of 2.5 mol% Pd, the sensor showed fast recovery time (5 s), high repeatability, long-term stability and excellent response (17.60) toward 3000 ppm of CH_4 at the operating temperature 340 °C [76]. A similar study was also reported for the Pd-SnO_2 gas sensor, which was fabricated by the sol-gel method, for the detection of CH_4 in the air [79]. Their experimental results exhibited that the addition of palladium causes a remarkable increase in the sensor response to CH_4 of about 6–7 times when compared with a pure tin dioxide sensor.

$R^2=0.9994$

$\beta=-17.30.e^{(-C/1775.97)}+20.79$

(a)

17.48
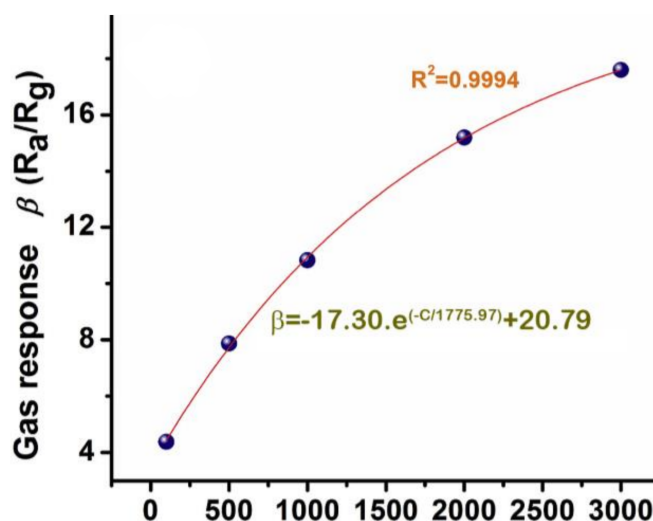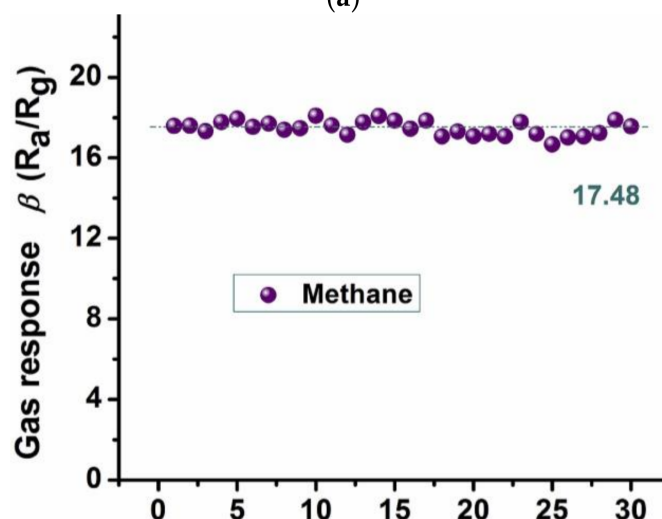
Methane

(b)

Figure 10. (**a**) The corresponding exponential correlation between the gas response and gas concentration; (**b**) stability state towards 3000 ppm of methane at 340 °C based on 2.5 mol% Pd-SnO$_2$ nanoporous composite. Reprinted with permission from reference [76].

Dongping Xue et al. [80] fabricated SnO$_2$-loaded WO$_3$ nanosheet composites and were able to detect CH$_4$ with a response time of about 1.4 times higher than pure tungsten trioxide at the optimum working temperature of 90 °C. Figure 11 shows the optimal operating temperature towards 500 ppm of CH$_4$. They observed that by raising the operating temperature up to 90 °C, the gas response was enhanced, while by a further increase in temperature, the sensor response decreased. γ-Fe$_2$O$_3$ nanoparticles were prepared using a green method for the detection of CH$_4$ with a concentration of 100 ppm at the operating temperature of 150 °C [81]. The results showed a higher response and selectivity, as well as a short response and recovery time in comparison with euphorbia extracted γ-Fe$_2$O$_3$ nanoparticles. Pt-VO$_x$ thin film obtained by the magnetron sputtering technique also showed a high sensing response towards 500 ppm of methane at room temperature [82].
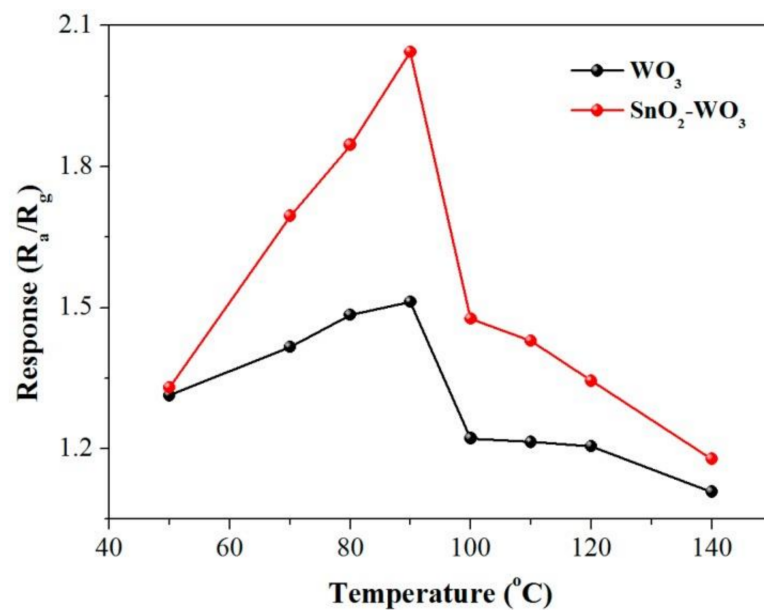
Figure 11. Gas response of pure tungsten trioxide and SnO_2-doped WO_3 towards 500 ppm of CH_4 at various working temperatures. Reprinted with permission from reference [80] under CC license.

Au-decorated vanadium dioxide nanosheets exhibited a good sensing response in presence of methane concentration in the range from 100 to 500 ppm at room temperature [83]. A gas sensor based on VO_2 nanoparticles was prepared by vapor transport method with a sensor response equal to 652 towards 500 ppm CH_4 concentration at 150 °C [84]. The cobalt-doped zirconium oxide exhibited a superior recovery time and response time of 27 s and 19 s, respectively, under 100 ppm methane with respect to the pure ZnO sensor [85]. The NiO decorated ZnO porous nanosheets showed high response and long-term stability too at 340 °C towards 1000 ppm of CH_4. These results were higher than that of pure ZnO porous nanosheets, due to the larger surface area and interfacial interaction of NiO and ZnO by p–n heterojunction formation [86]. A summary of metal oxide semiconductor-based CH_4 gas sensors is reported in Table 5.

Table 5. A brief summary of MOX-based CH_4 gas sensors.

Material	Structure/Synthesis Method	Target Gas/ Concentration (ppm)	Operating T (°C)	Response (%)	Ref.
TiO_2	nanorods/hydrothermal	CH_4/60	RT	6028	[87]
		CH_4/5		987	
Cd/TiO_3	thin films/magnetron co-sputtering	CH_4/500	250	3.4	[88]
VO_2	nanorods/thermal evaporation	CH_4/500	RT	35	[89]
V_2O_5	nano-flowers/magnetron sputtering	CH_4/500	100	11.2	[90]
	nano-rods			8.9	
	nano-urchins			9.1	
Au/VO_2	nanosheets/CVD, ion sputtering	CH_4/500	RT	~70	[83]
SnO_2	nanoparticles/sol-gel	CH_4/20,000	80	~3.5	[91]

Table 5. *Cont.*

Material	Structure/Synthesis Method	Target Gas/ Concentration (ppm)	Operating T (°C)	Response (%)	Ref.
SnO_2	quantum dots/sonication assisted precipitation	CH_4/5000	>375	~100	[92]
SnO_2/WO_3	nanosheets/impregnation	CH_4/500	90	~2	[80]
WO_3	nanosheets/hydrothermal			~1.5	
Pd/SnO_2	hollow spheres/adsorption– calcination	CH_4/250	300	4.88	[93]
SnO_2	hollow spheres/progressive inward crystallization routine		400	1.31	
SnO_2/NiO	porousnanosheets/immersion- calcination	CH_4/500	330	15.2	[94]
ZnO/rGO	nanorods, nanosheets/hydrothermal	CH_4/100–4000	190	4.52	[95]
ZnO/NiO	porous nanosheets/hydrothermal, post-treatment	CH_4/1000	340	34.2	[86]
Pd/SnO_2	nanoporous/hydrothermal	CH_4/3000	340	17.6	[76]
NiO/Al	thin films/RF sputtering	CH_4/100	RT	58	[96]
ZnO	nanoporous/electrochemical deposition	CH_4/100	220	~4.8	[97]
ZnO	nanowalls/thermal evaporation	CH_4/100	300	8.1	[98]
Co/ZnO	nanoparticles/solvothermal	CH_4/100	140	1.05	[99]
α-Fe_2O_3	nanoparticles/commercial	CH_4/4000	RT	1.08	[100]
$\alpha Fe_{1.92}$/$Cu_{0.08}O_3$	nanoparticles/homogenous co-precipitation			1.12	

CDV = chemical vapor transport deposition; RT = room temperature; rGO = reduced graphene oxide; RF = radio frequency.

3.3. Sensing of Nitrous Oxide Gas

Another important greenhouse gas is nitrous oxide (N_2O), which is a colorless gas with a sweet odor. The World Meteorological Organization reported that N_2O concentration in air was 333.2 ± 0.1 ppb in 2020 which was 123% more with respect to pre-industrial levels. The increase of N_2O from 2018 to 2019 was comparable with the average growth rate over the last decade (+0.99 ppb/y), although the increase of nitrous gases in these years was lower than reported results between 2017 and 2018 [75]. For these reasons, it is very important to develop gas sensor for N_2O for the protection of humans' health and the environment. Nevertheless, there is a relatively small body of literature on the use of metal oxide semiconductor-based sensors towards N_2O detection.

Among the MOX-based gas sensors, several researchers reported SnO_2 and WO_3 for N_2O detection. In_2O_3 based gas sensors provide noticeably sensing properties for the N_2O detection too. WO_3 nanowire mats and nanoparticle films were obtained by HF-CVD technique (hot filament chemical vapor deposition) and showed a good sensitivity towards N_2O in the operating temperature range 100–500 °C [101]. In comparison with nanoparticle films, by increasing the temperature, the mat-like nanowire network provided higher sensitivity with response time and recovery time of 75 s and 360 s, respectively, at about 450 °C; 0.5 wt% Sm_2O_3-loaded SnO_2 nanopowders were produced by the electrochemical route and showed high sensitivity towards 35 ppm of N_2O in air. The experimental results

highlighted that, by introducing Sm_2O_3, sensitivity increased up to approximately 1.5 times higher than pure SnO_2 [102]. The sensing characteristics of nanowire indium oxide and tungsten trioxide were investigated by Rout et al. [103]. The In_2O_3 nanowire (~20 nm in diameter) sensor showed a response and recovery time of about 20 s along with a sensor response of 60 in the presence of 10 ppm N_2O at 150 °C, whereas WO_3 nanowire (5–15 nm in diameter)-based sensors exhibited a sensor response of 20–25 with a response and recovery times of 10 s and 60 s, respectively, under 10 ppm N_2O at 250 °C. They reported that the sensitivity of indium oxide and tungsten trioxide nanowires is not affected in the presence of water vapor, up to 90% relative humidity. SrO-doped SnO_2 demonstrated higher sensitivity and response time (three times) under 10–300 ppm N_2O at 500 °C than pure SnO_2 [38]. Table 6 summarizes the reported results in the literature on MOX-based N_2O gas sensors.

Table 6. Summary of MOX-based nitrous oxide gas sensors.

Material	Structure/Synthesis Method	Target Gas/ Concentration (ppm)	Operating T (°C)	Sensitivity	Ref.
BaO/SnO_2	co-precipitation	$N_2O/300$	500	3	[38]
Sm_2O_3/SnO_2				3	
PbO/SnO_2				2.5	
Gd_2O_3/SnO_2				2.7	
SrO/SnO_2	co-precipitation	$N_2O/300$	450	1.66	
			500	4.5	
In_2O_3	nanowires/carbothermal	$N_2O/10$	250	~5	[103]
WO_3	nanowires/solvothermal			25	
ZnO	nanorods/self-assembly of ZnO nanodots			~5	
Au/SnO_x	films/L-MOCVD	$N_2O/100$	210	11.5	[104]
SnO_2		$N_2O/300$	450	1.66	

L-MOCVD = laser-induced metal–organic chemical vapor deposition; RT = room temperature.

3.4. Fluorinated Gases (HFCs, PFCs and SF₆)

In the 19th century, the levels of methane were stable at 34.1 ± 0.3 ppt (part per trillion), while for both C_2F_6 and C_3F_8 gasses, they were below detection limits of 0.002 and 0.01 ppt, respectively. Around 1940, due to the high production of aluminum because of World War II, peaks corresponding to the emission of CF_4 and C_2F_6 were detected. Furthermore, the emissions of PFCs were drastically decreased for CF_4 (in 1980) and C_2F_6 and C_3F_8 (early to mid-2000s), but they then slowed down and probably stopped recently [8]. Due to their low concentration, these gases can be detected with good accuracy by gas chromatography with electron capture detector (GC/ECD). Figure 12 shows the baseline of fluorinated gas emission from 2005 to 2050. As can be seen, the emissions of F-gases are estimated to increase five times in this period. This increase can be described by a sixfold enhancement in the demand for air conditioners and refrigeration services, especially in developing countries, along with the effect of the replacement of CFCs and HCFCs with HFCs. A growth of 25% is expected for PFC emissions over the same period because of industry development and emission contractions in primary aluminum production. It is expected that SF_6 emissions will enhance too (by almost 50%), owing to the increase in emissions from high and medium voltage switches as a result of the increase in electricity consumption and the development of magnesium production [6].

SF_6 has been extensively applied in gas-insulated high-voltage switchgear (GIS, a compact metal encapsulated switchgear made of high-voltage components which can be safely operated in confined spaces) [105]. Due to partial discharge fault, sulfur hexafluoride

decomposes, resulting in the generation of different low-fluoride sulfides. The reaction of low-fluoride sulfides with H_2O and O_2 in gas-insulating equipment leads to the production of different decomposition products such as SO_2, H_2S, SOF_2 and SO_2F_2. In order to assess the operating state and insulation level of GIS, the partial discharge detection and analysis of content and composition of SF_6 gas components have significant importance [106]. To this aim, the development of gas sensing equipment able to detect SF_6 decomposition products can be considered as a proper way for online monitoring of partial discharge fault in GIS.
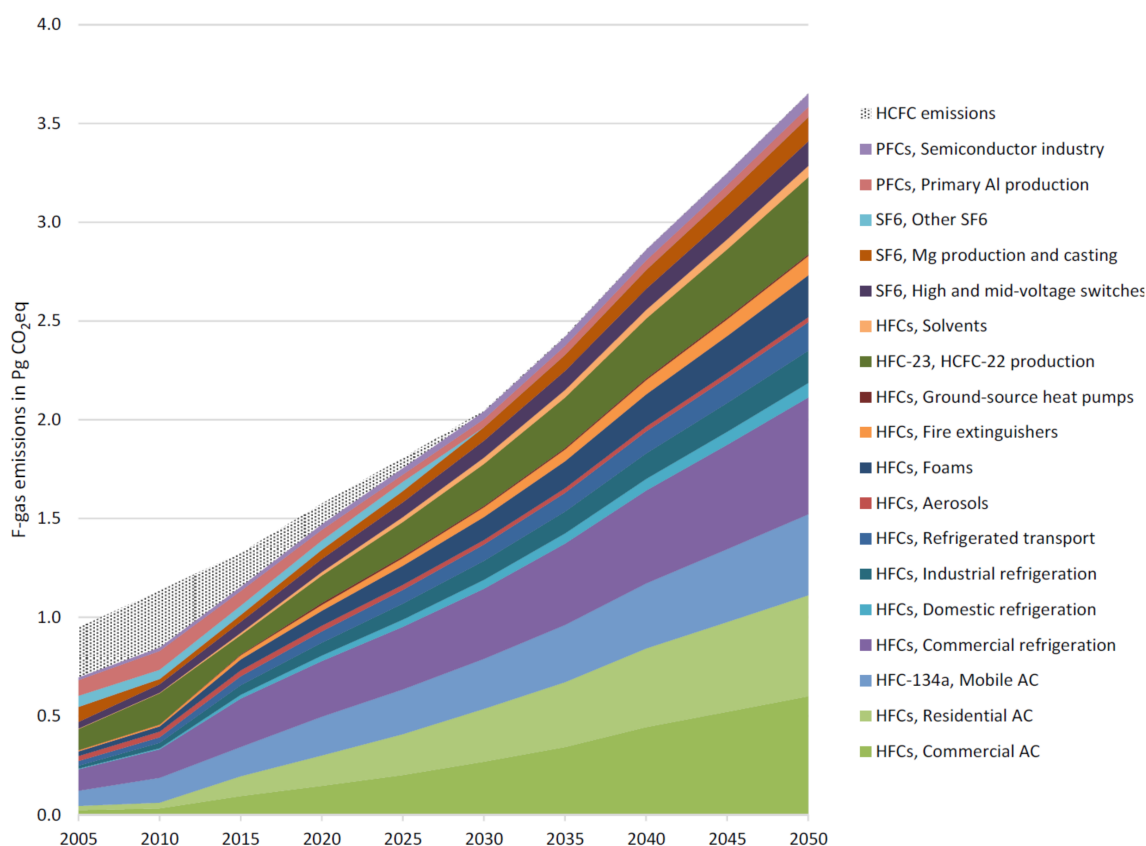

Figure 12. Baseline fluorinated gases (HFCs, PFCs, and SF_6) by source sector from 2005 to 2050 [107] under CC license.

Hongcheng Liu et al. [108] produced pure and NiO-decorated ZnO nanoflowers by the hydrothermal process for the detection of SF_6 decomposition products (SO_2, SO_2F_2, and SOF_2). They reported that, by the addition of NiO, the properties of the ZnO-based sensor clearly increased, such as higher gas response, lower optimal operating temperature and shorter response and recovery time. Table 7 presents a brief summary of reported results on MOX-based sensors for the detection of decomposition products of sulfur hexafluoride.

Au modified (1.2 at%) ZnO nanowires prepared by hydrothermal synthesis showed a high response (79.4) to 5 ppm H_2S at room temperature in reference [109] due to the formation of nano-Schottky type barrier junctions at the interface between 5 nm Au particles and ZnO nanorods.

Table 7. Summary of MOX-based sensor towards SF_6 decomposed products.

Material	Structure/Synthesis Method	Target Gas/ Concentration (ppm)	Operating T (°C)	Response (%)	Ref.
NiO/ZnO	nanoflowers/hydrothermal	SO_2, SOF_2, SO_2F_2/100	260	SO_2 (33.35) SOF_2 (22.25) SO_2F_2 (36.67)	[108]
Au/ZnO	nanowires/hydrothermal	H_2S/1	RT	38	[109]
In_2O_3	nanowires/chemical vapor deposition	H_2S/1	RT	30.4	[110]
In_2O_3	single crystal whisker/carbothermal method	H_2S/200 ppb	RT	47.9	[111]
CuO	nanowires/resistive heating of Cu wires	H_2S/10 ppb	325	40.9	[112]
ZnO	flower-like nanorods/ hydrothermal	SO_2, SOF_2, SO_2F_2/10 (μL/L)	(SO_2)250 (SOF_2 and SO_2F_2) 300	SO_2 (-33.44) SOF_2 (-12.47) SO_2F_2 (-18.06)	[113]
TiO_2	nanotube array/anodic oxidation	SO_2, SOF_2, SO_2F_2/50	200	SO_2 (-76) SOF_2 (-7.8) SO_2F_2 (-5.5)	[114]
CuO/WO_3	nanowires/thermal evaporation followed sputter-deposition, thermal annealing	H_2S/100	300	6.72	[115]
TiO_2	nanotube array/anodic oxidation	SO_2, SOF_2, SO_2F_2/50	110	SO_2 (-74.6) SOF_2 (-7.82) SO_2F_2 (-5.52)	[116]
Au/TiO_2	nanotube array/ deposition-precipitation	SO_2, SOF_2, SO_2F_2/50	110	SO_2F_2 (-19.95) SOF_2 (-9.97) SO_2 (-8.73)	
$TiO_2/NiSO_4$	nanofibers/electrospun, hydrothermal	SO_2F_2/100	RT	189	[117]
SnO_2	microspheres/hydrothermal	SO_2/30	300	43.15	[118]
Cu/SnO_2	microspheres/conventionalindirect heating		275	23.37	
Fe_2O_3/NiO	nanoplates/solvothermal	H_2S/50	200	26.48	[119]
Pt/TiO_2	nanotube arrays/pulse electrodeposition	SO_2, SOF_2, SO_2F_2/50	150	SO_2 (8.38) SOF_2 (6.11) SO_2F_2 (17.91)	[120]
ZnO/SnO_2	nanofibers/electrospinning	H_2S/50	250	66.23	[121]
WO_3/NiO	nanoflowers/hydrothermal	H_2S/20	160	33.34	[122]

H_2S has strong electron-accepting capacities and can be detected by In_2O_3 nanowire (80 nm in diameter) transistors down to 1 ppm at room temperature with reasonably fast response and recovery times (48 s and 56 s, respectively, when switching the atmosphere from under air to 1 ppm of H_2S and vice versa) [110]. Single crystal whiskers and thick films of bipyramids of cubic In_2O_3 were grown by carbothermal method in reference [111] and showed that the single crystal whiskers were selective and could be used to detect 200 ppb of H_2S while bipyramids films could be used in a 10–80 ppm range of hydrogen sulphide at room temperature. The lower detection limit of single crystal whiskers with respect to bipyramid crystals was attributed to a higher presence of singly charged oxygen vacancy defects.

Conductimetric sensors based on a suspended single CuO nanowire were able to sense H_2S in dry and humid atmosphere (65 RH%) down to 10 ppb at 325 °C in reference [112]. Suspended nanowires are in a highly favorable configuration because they can be fully immersed in the gas atmosphere. Humidity-induced Debye length modulation was probably small compared to the large nanowire diameter (170 nm) thus, no evident increase or decrease of the resistance was evidenced when testing the sensors either in a dry or humid environment. These results are promising in view of the integration of CuO nanowires on CMOS-fabricated micro-hotplates to achieve miniaturized, low power consumption portable devices.

4. Conclusions and Perspectives

Accurate measurements and reliable quantifications of anthropogenic GHG emissions in air are of primary importance to study climate change and for taking mitigation actions. In this review, the general properties and gas sensing mechanisms of semiconductor metal oxides were first presented. Then, the factors that influence their sensitivity, selectivity and stability were also illustrated. Because of GHG concentration in air, MOX gas sensors have the potential to detect mainly CO_2, CH_4, N_2O and PFC decomposition products in GIS in remote monitoring systems.

In the case of CO_2 detection in air, MOX gas sensors already show the sensor response and the LOD compatible with the targeted application from room temperature and up to 400 °C operating temperatures. Their cross-sensitivity needs, however, to be fully evaluated (for example, ZnO sensors can detect almost all the above-cited GHGs (Tables 4–7)). Humidity strongly interferes when doing measurements in air. The core@shell structure based on ZnO nanowire-zeolite imidazole framework (ZIF) array could be investigated for GHG sensors with an improved selectivity with respect to water vapor.

Direct growth techniques of vertically oriented ZnO nanomaterials on electrode surfaces appear to be interesting manufacturing processes and allow the miniaturization of sensors and their incorporation in remote monitoring systems. The surface functionalization of vertically aligned ZnO nanomaterials with specific metal catalysts, dopants, and other metal oxides is a promising approach for improving sensing response, selectivity and response/recovery time too [123]. However, their ageing behavior has also to be studied: according to our experience in CO_2 detection with ZnO screen-printed sensors, the sensor's response significantly decreases after one year of intermittent operation at 200 °C. Thus, other 1D nanomaterials have to be investigated for the detection of GHGs.

Methane monitoring is also of utmost importance since the COP26 in Glasgow and the Global Methane Pledge signed up to by more than 100 countries. The MOX gas sensors can detect CH_4 in the concentration range from 60 to 20,000 ppm in the working temperature range from room temperature to 500 °C (Table 5). However, much effort will be needed to detect methane in air (targeting the 2 ppm current atmospheric concentration). The development of new nanocomposites could be the successful key to target this aim.

Nitrous oxide detection by means of MOX gas sensors is effective in the range 10–300 ppm at 200–500 °C (Table 6). For N_2O detection in air, the sensor response and the LOD must be significantly improved too (the target is about 0.3 ppm). Moreover, for this application, significant improvements can be expected from new nanocomposite developments.

Finally, sulfur hexafluoride decomposition products such as SO_2, H_2S, SOF_2 and SO_2F_2 can be evidenced by means of MOX gas sensors (Table 7). Even if concentrations of 20–100 ppm of these gases can be already detected, these performances could be considered as satisfying because GIS are compact metal encapsulated systems and the measurements are done in a closed environment and not in air. However, conductimetric sensors showed a lower limit of detection with respect to resistive semiconducting metal oxides and allowed the detection of hydrogen sulfide concentrations as low as 10 ppb at 325 °C.

Author Contributions: Both authors contributed equally. All authors have read and agreed to the published version of the manuscript.

References

1. Villar, J.C.; Hidalgo, S.L.; Penela, A.C.; Meijide, B.G. A New Perspective for Labeling the Carbon Footprint against Climate Change. In *Global Warming—Impacts and Future Perspective*; Bharat, R.S., Ed.; InTech: Rijeka, Croatia, 2012.
2. Solomon, S.; Qin, D.; Manning, M.; Chen, Z.; Marquis, M.; Averyt, K.B.; Tignor, M.; Miller, H.L. *Climate Change 2007: The Physical Science Basis. Contribution of Working Group I to the Fourth Assessment Report of the Intergovernmental Panel on Climate Change*; Cambridge University Press: Cambridge, UK; Cambridge University Press: New York, NY, USA, 2007.
3. World Meteorological Organization. *WMO Greenhouse Gas Bulletin, No. 16*; WMO: Geneva, Switzerland, 2020.
4. Santhanam, K.S.V.; Ahamed, N.N.N. Greenhouse Gas Sensors Fabricated with New Materials for Climatic Usage: A Review. *ChemEngineering* **2018**, *2*, 38. [CrossRef]
5. Stocker, T.F.; Qin, D.; Plattner, G.-K.; Tignor, M.B.M.; Allen, S.K.; Boschung, J.; Nauels, A.; Xia, Y.; Bex, P.M.M.V. *Climate Change 2013 The Physical Science Basis: Working Group I Contribution to the Fifth Assessment Report of the Intergovernmental Panel on Climate Change*; Cambridge University Press: Cambridge, UK, 2013.
6. Sonker, R.K.; Sabhajeet, S.R.; Yadav, B.C. TiO$_2$–PANI nanocomposite thin film prepared by spin coating technique working as room temperature CO$_2$ gas sensing. *J. Mater. Sci. Mater. Electron.* **2016**, *27*, 11726–11732. [CrossRef]
7. Rauh, F.; Schwenk, M.; Pejcic, B.; Myers, M.; Ho, K.-B.; Stalker, L.; Mizaikoff, B. A mid-infrared sensor for the determination of perfluorocarbon-based compounds in aquatic systems for geosequestration purposes. *Talanta* **2014**, *130*, 527–535. [CrossRef]
8. Trudinger, C.M.; Fraser, P.J.; Etheridge, D.M.; Sturges, W.T.; Vollmer, M.K.; Rigby, M.; Martinerie, P.; Mühle, J.; Worton, D.R.; Krummel, P.B.; et al. Atmospheric abundance and global emissions of perfluorocarbons CF4, C2F6 and C3F8 since 1800 inferred from ice core, firn, air archive and in situ measurements. *Atmos. Chem. Phys.* **2016**, *16*, 11733–11754. [CrossRef]
9. US Energy Information Administration (EIA). *Energy and the Environment Explained Greenhouse Gases*; US Energy Information Administration (EIA): Washington, DC, USA, 2021.
10. Berrou, A.; Raybaut, M.; Godard, A.; Lefebvre, M. High-resolution photoacoustic and direct absorption spectroscopy of main greenhouse gases by use of a pulsed entangled cavity doubly resonant OPO. *Appl. Phys. A* **2009**, *98*, 217–230. [CrossRef]
11. PBL Netherlands Environmental Assessment Agency. Growth of 1.1% in Global Greenhouse Gas Emissions in 2019. Available online: Https://www.pbl.nl/en/news/2020/growth (accessed on 5 December 2021).
12. Oertel, C.; Matschullat, J.; Zurba, K.; Zimmermann, F.; Erasmi, S. Greenhouse Gas Emissions from Soils—A Review. *Geo-Chem.* **2016**, *76*, 327–352. [CrossRef]
13. Gautam, Y.K.; Sharma, K.; Tyagi, S.; Ambedkar, A.K.; Chaudhary, M.; Pal Singh, B. Nanostructured Metal Oxide Semicon-ductor-Based Sensors for Greenhouse Gas Detection: Progress and Challenges. *R. Soc. Open Sci.* **2021**, *8*, 201324. [CrossRef]
14. Meld. St. Longship—Carbon Capture and Storage. Available online: https://www.regjeringen.no/en/dokumenter/meld.-st.-33-20192020/id2765361/ (accessed on 5 December 2021).
15. Olaniyi, O.A.; Ojekunle, Z.O.; Amujo, B.T. Review of Climate Change and Its Effect on Nigeria Ecosystem. *Int. J. Afr. Asian Stud. Open Access Int. J.* **2013**, *1*, 57–65.
16. Jaaniso, R.; Kiang Tan, O. *Semiconductor Gas Sensors*; Woodhead Publishing Series in Electronic and Optical Materials; Woodhead Publishing Limited: Oxford, UK, 2013.
17. Arshak, K.; Moore, E.; Lyons, G.M.; Harris, J.; Clifford, S. A review of gas sensors employed in electronic nose applications. *Sens. Rev.* **2004**, *24*, 181–198. [CrossRef]
18. Shankar, P.; Rayappan, J.B.B. Gas Sensing Mechanism of Metal Oxides: The Role of Ambient Atmosphere, Type of Semicon-ductor and Gases—A Review. *Sci. Lett. J.* **2015**, *4*, 126.
19. Wetchakun, K.; Samerjai, T.; Tamaekong, N.; Liewhiran, C.; Siriwong, C.; Kruefu, V.; Wisitsoraat, A.; Tuantranont, A.; Phanich-phant, S. Semiconducting metal oxides as sensors for environmentally hazardous gases. *Sens. Actuators B Chem.* **2011**, *160*, 580–591. [CrossRef]
20. Fine, G.F.; Cavanagh, L.M.; Afonja, A.; Binions, R. Metal Oxide Semi-Conductor Gas Sensors in Environmental Monitoring. *Sensors* **2010**, *10*, 5469–5502. [CrossRef] [PubMed]
21. Barsan, N.; Weimar, U. Conduction Model of Metal Oxide Gas Sensors. *J. Electroceram.* **2001**, *7*, 143–167. [CrossRef]
22. Bapathi, K.S.R.; Pramod, H. Borse Review—Recent Material Advances and Their Mechanistic Approaches for Room Temperature Chemiresistive Gas Sensors. *Electrochem. Soc.* **2021**, *168*, 057521.
23. Tofield, P.T.M.B.C. *Solid State Gas Sensors*; Adam Hilger: Bristol, UK, 1987.
24. Sberveglieri, G. *Gas Sensors*; Kluwer Academic Publishing: Berlin, Germany, 1992.
25. Azad, A.M.; Akbar, S.A.; Mhaisalkar, S.; Birkefeld, L.D.; Goto, K.S. Solid-State Gas Sensors: A Review. *J. Electrochem. Soc.* **1992**, *139*, 3690–3704. [CrossRef]

26. Barsan, N.; Schweizer-Berberich, M.; Göpel†, W. Fundamental and practical aspects in the design of nanoscaled SnO_2 gas sensors: A status report. *Anal. Bioanal. Chem.* **1999**, *365*, 287–304. [CrossRef]

27. Kim, H.J.; Lee, J.H. Highly Sensitive and Selective Gas Sensors Using P-Type Oxide Semiconductors: Overview. *Sens. Actuators B Chem.* **2014**, *192*, 607–627. [CrossRef]

28. Wang, C.; Yin, L.; Zhang, L.; Xiang, D.; Gao, R. Metal Oxide Gas Sensors: Sensitivity and Influencing Factors. *Sensors* **2010**, *10*, 2088–2106. [CrossRef]

29. Yamazoe, N. New approaches for improving semiconductor gas sensors. *Sens. Actuators B Chem.* **1991**, *5*, 7–19. [CrossRef]

30. Korotcenkov, G. New Trends and Technologies. In *Handbook of Gas Sensor Materials: Properties, Advantages, and Shortcomings for Applications*; Springer: New York, NY, USA, 2014; Volume 2.

31. Korotcenkov, G. Conventional Approaches. In *Handbook of Gas Sensor Materials Properties, Advantages and Shortcomings for Applications*; Springer: New York, NY, USA, 2013; Volume 1.

32. Dey, A. Semiconductor metal oxide gas sensors: A review. *Mater. Sci. Eng. B* **2018**, *229*, 206–217. [CrossRef]

33. Nikolic, M.V.; Milovanovic, V.; Vasiljevic, Z.Z.; Stamenkovic, Z. Semiconductor Gas Sensors: Materials, Technology, Design, and Application. *Sensors* **2020**, *20*, 6694. [CrossRef] [PubMed]

34. Korotcenkov, G.; Cho, B. Metal oxide composites in conductometric gas sensors: Achievements and challenges. *Sens. Actuators B Chem.* **2017**, *244*, 182–210. [CrossRef]

35. Staerz, A.; Berthold, C.; Russ, T.; Wicker, S.; Weimar, U.; Barsan, N. The oxidizing effect of humidity on WO3 based sensors. *Sens. Actuators B Chem.* **2016**, *237*, 54–58. [CrossRef]

36. Glebov, A.; Graham, A.P.; Menzel, A.; Toennies, J.P. Orientational ordering of two-dimensional ice on Pt(111). *J. Chem. Phys.* **1997**, *106*, 9382–9385. [CrossRef]

37. Feibelman, P.J. Reactive Wetting: H2O/Rh(111). *Phys. Rev. Lett.* **2003**, *90*, 186103. [CrossRef] [PubMed]

38. Kanazawa, E.; Sakai, G.; Shimanoe, K.; Kanmura, Y.; Teraoka, Y.; Miura, N.; Yamazoe, N. Metal oxide semiconductor N_2O sensor for medical use. *Sens. Actuators B Chem.* **2001**, *77*, 72–77. [CrossRef]

39. Krivetskiy, V.; Ponzoni, A.; Comini, E.; Badalyan, S.; Rumyantseva, M.; Gaskov, A. Selectivity Modification of SnO_2-Based Materials for Gas Sensor Arrays. *Electroanalysis* **2010**, *22*, 2809–2816. [CrossRef]

40. Patil, S.J.; Patil, A.V.; Dighavkar, C.G.; Thakare, K.S.; Borase, R.Y.; Nandre, S.J.; Deshpande, N.G.; Ahire, R.R. Semiconductor metal oxide compounds based gas sensors: A literature review. *Front. Mater. Sci.* **2015**, *9*, 14–37. [CrossRef]

41. Basyooni, M.A.; Shaban, M.; El Sayed, A.M. Enhanced Gas Sensing Properties of Spin-coated Na-doped ZnO Nanostructured Films. *Sci. Rep.* **2017**, *7*, srep41716. [CrossRef]

42. Available online: Https://Gml.Noaa.Gov/Webdata/Ccgg/Trends/Co2_data_mlo.Png (accessed on 5 December 2021).

43. Available online: Https://Gml.Noaa.Gov/Ccgg/Trends/Mlo.Html (accessed on 5 December 2021).

44. Cozzi, L. *Energy and Air Pollution, World Energy Outlook Special Report OECD/IEA*; International Energy Agency: Paris, France, 2016.

45. Cole, S.; Ellen, E. *New NASA Satellite Maps Show Human Fingerprint on Global Air Quality*; National Aeronautical Space Administration (NASA): Washington, DC, USA, 2015.

46. Çolak, H.; Karaköse, E. Synthesis and Characterization of Different Dopant (Ge, Nd, W)-Doped ZnO Nanorods and Their CO_2 Gas Sensing Applications. *Sens. Actuators B Chem.* **2019**, *296*, 126629. [CrossRef]

47. Shohany, B.G.; Motevalizadeh, L.; Abrishami, M.E. Investigation of ZnO thin-film sensing properties for CO_2 detection: Effect of Mn doping. *J. Theor. Appl. Phys.* **2018**, *12*, 219–225. [CrossRef]

48. Hunge, Y.M.; Yadav, A.A.; Kulkarni, S.B.; Mathe, V.L. A Multifunctional ZnO Thin Film Based Devices for Photoelectrocat-alytic Degradation of Terephthalic Acid and CO_2 Gas Sensing Applications. *Sens. Actuators B Chem.* **2018**, *274*, 1–9. [CrossRef]

49. Habib, M.; Hussain, S.S.; Riaz, S.; Naseem, S. Preparation and Characterization of ZnO Nanowires and their Applications in CO_2 Gas Sensors. *Mater. Today Proc.* **2015**, *2*, 5714–5719. [CrossRef]

50. Aboud, A.A.; Al-Kelesh, H.; El Rouby, W.; Farghali, A.; Hamdedein, A.; Khedr, M.H. CO_2 responses based on pure and doped CeO_2 nano-pellets. *J. Mater. Res. Technol.* **2018**, *7*, 14–20. [CrossRef]

51. Jeong, Y.-J.; Balamurugan, C.; Lee, D.-W. Enhanced CO_2 gas-sensing performance of ZnO nanopowder by La loaded during simple hydrothermal method. *Sens. Actuators B Chem.* **2016**, *229*, 288–296. [CrossRef]

52. Dhahri, R.; Hjiri, M.; El Mir, L.; Fazio, E.; Neri, F.; Barreca, F.; Donato, N.; Bonavita, A.; Leonardi, S.G.; Neri, G. ZnO: Ca Nanopowders with Enhanced CO_2 Sensing Properties. *J. Phys. D. Appl. Phys.* **2015**, *48*, 255503. [CrossRef]

53. Ghosh, A.; Zhang, C.; Shi, S.; Zhang, H. High temperature CO_2 sensing and its cross-sensitivity towards H_2 and CO gas using calcium doped ZnO thin film coated langasite SAW sensor. *Sens. Actuators B Chem.* **2019**, *301*, 126958. [CrossRef]

54. Joshi, S.; Ippolito, S.J.; Periasamy, S.; Sabri, Y.M.; Sunkara, M. V Efficient Heterostructures of Ag@ CuO/BaTiO3 for Low-Temperature CO_2 Gas Detection: Assessing the Role of Nanointerfaces during Sensing by Operando DRIFTS Technique. *ACS Appl. Mater. Interfaces* **2017**, *9*, 27014–27026. [CrossRef]

55. Abdelmounaïm, C.; Amara, Z.; Maha, A.; Mustapha, D. Effects of molarity on structural, optical, morphological and CO_2 gas sensing properties of nanostructured copper oxide films deposited by spray pyrolysis. *Mater. Sci. Semicond. Process.* **2016**, *43*, 214–221. [CrossRef]

56. Deepa, S.; Kumari, K.P.; Thomas, B. Contribution of oxygen-vacancy defect-types in enhanced CO_2 sensing of nanoparticulate Zn-doped SnO_2 films. *Ceram. Int.* **2017**, *43*, 17128–17141. [CrossRef]

57. Raulkar, K. Study on sensitivity of nano SnO$_2$ -ZnO composites with and without PPy layer for sensing CO$_2$ gas. *Mater. Today. Proc.* **2019**, *15*, 604–610. [CrossRef]

58. Hsu, K.-C.; Fang, T.-H.; Hsiao, Y.-J.; Chan, C.-A. Highly Response CO$_2$ Gas Sensor Based on Au-La$_2$O$_3$ Doped SnO$_2$ Nano-fibers. *Mater. Lett.* **2020**, *261*, 127144. [CrossRef]

59. Xiong, Y.; Zhang, G.; Zhang, S.; Zeng, D.; Xie, C. Tin oxide thick film by doping rare earth for detecting traces of CO$_2$: Operating in oxygen-free atmosphere. *Mater. Res. Bull.* **2014**, *52*, 56–64. [CrossRef]

60. Krishnakumar, T.; Jayaprakash, R.; Prakash, T.; Sathyaraj, D.; Donato, N.; Licoccia, S.; Latino, M.; Stassi, A.; Neri, G. CdO-based nanostructures as novel CO$_2$ gas sensors. *Nanotechnology* **2011**, *22*, 325501. [CrossRef] [PubMed]

61. Rajesh, N.; Kannan, J.; Krishnakumar, T.; Bonavita, A.; Leonardi, S.G.; Neri, G. Microwave irradiated Sn-substituted CdO nanostructures for enhanced CO$_2$ sensing. *Ceram. Int.* **2015**, *41*, 14766–14772. [CrossRef]

62. Prim, A.; Pellicer, E.; Rossinyol, E.; Peiró, F.; Cornet, A.; Morante, J.R. A Novel Mesoporous CaO-Loaded In$_2$O$_3$ Material for CO$_2$ Sensing. *Adv. Funct. Mater.* **2007**, *17*, 2957–2963. [CrossRef]

63. Michel, C.; Martínez-Preciado, A.H.; Rivera-Tello, C.D. CO$_2$ gas sensing response of YPO4 nanobelts produced by a colloidal method. *Sens. Actuators B Chem.* **2015**, *221*, 499–506. [CrossRef]

64. Yadav, A.A.; Lokhande, A.C.; Kim, J.H.; Lokhande, C.D. Highly sensitive CO$_2$ sensor based on microrods-like La$_2$O$_3$ thin film electrode. *RSC Adv.* **2016**, *6*, 106074–106080. [CrossRef]

65. Zhang, W.; Xie, C.; Zhang, G.; Zhang, J.; Zhang, S.; Zeng, D. Porous LaFeO$_3$/SnO$_2$ Nanocomposite Film for CO$_2$ Detection with High Sensitivity. *Mater. Chem. Phys.* **2017**, *186*, 228–236. [CrossRef]

66. Wang, X.; Qin, H.; Sun, L.; Hu, J. CO$_2$ sensing properties and mechanism of nanocrystalline LaFeO$_3$ sensor. *Sens. Actuators B Chem.* **2013**, *188*, 965–971. [CrossRef]

67. Yadav, A.; Lokhande, A.; Kim, J.; Lokhande, C. Improvement in CO$_2$ sensing characteristics using Pd nanoparticles decorated La$_2$O$_3$ thin films. *J. Ind. Eng. Chem.* **2017**, *49*, 76–81. [CrossRef]

68. Mardare, D.; Cornei, N.; Mita, C.; Florea, D.; Stancu, A.; Tiron, V.; Manole, A.; Adomnitei, C. Low temperature TiO$_2$ based gas sensors for CO$_2$. *Ceram. Int.* **2016**, *42*, 7353–7359. [CrossRef]

69. Karaduman, I.; Demir, M.; Yıldız, D.E.; Acar, S. CO$_2$gas detection properties of a TiO$_2$/Al$_2$O$_3$heterostructure under UV light irradiation. *Phys. Scr.* **2015**, *90*, 55802. [CrossRef]

70. Yao, M.-S.; Tang, W.-X.; Wang, G.-E.; Nath, B.; Xu, G. MOF Thin Film-Coated Metal Oxide Nanowire Array: Significantly Improved Chemiresistor Sensor Performance. *Adv. Mater.* **2016**, *28*, 5229–5234. [CrossRef] [PubMed]

71. Basyooni, M.A.; Zaki, S.E.; Ertugrul, S.; Yilmaz, M.; Eker, Y.R. Fast response of CO$_2$ room temperature gas sensor based on Mixed-Valence Phases in Molybdenum and Tungsten Oxide nanostructured thin films. *Ceram. Int.* **2019**, *46*, 9839–9853. [CrossRef]

72. Tanvir, N.B.; Yurchenko, O.; Laubender, E.; Pohle, R.; Sicard, O.V.; Urban, G. Zinc Peroxide Combustion Promoter in Prepa-ration of CuO Layers for Conductometric CO$_2$ Sensing. *Sens. Actuators B Chem.* **2018**, *257*, 1027–1034. [CrossRef]

73. Rudraswamy, S.B.; Bhat, N. Optimization of RF Sputtered Ag-Doped BaTiO$_3$-CuO Mixed Oxide Thin Film as Carbon Dioxide Sensor for Environmental Pollution Monitoring Application. *IEEE Sens. J.* **2016**, *16*, 5145–5151. [CrossRef]

74. Herrán, J.; Fernández-González, O.; Castro-Hurtado, I.; Romero, T.; Mandayo, G.G.; Castaño, E. Photoactivated solid-state gas sensor for carbon dioxide detection at room temperature. *Sens. Actuators B Chem.* **2010**, *149*, 368–372. [CrossRef]

75. Available online: Https://Public.Wmo.Int/En/Media/Press-Release/Carbon-Dioxide-Levels-Continue-Record-Levels-despite-Covid-19-Lockdown (accessed on 5 December 2021).

76. Yao, L.; Li, Y.; Ran, Y.; Yang, Y.; Zhao, R.; Su, L.; Kong, Y.; Ma, D.; Chen, Y.; Wang, Y. Construction of novel Pd–SnO$_2$ composite nanoporous structure as a high-response sensor for methane gas. *J. Alloy. Compd.* **2020**, *826*, 154063. [CrossRef]

77. Lu, W.; Ding, D.; Xue, Q.; Du, Y.; Xiong, Y.; Zhang, J.; Pan, X.; Xing, W. Great enhancement of CH$_4$ sensitivity of SnO$_2$ based nanofibers by heterogeneous sensitization and catalytic effect. *Sens. Actuators B Chem.* **2018**, *254*, 393–401. [CrossRef]

78. Bunpang, K.; Wisitsoraat, A.; Tuantranont, A.; Singkammo, S.; Phanichphant, S.; Liewhiran, C. Highly selective and sensitive CH$_4$ gas sensors based on flame-spray-made Cr-doped SnO$_2$ particulate films. *Sens. Actuators B Chem.* **2019**, *291*, 177–191. [CrossRef]

79. Fedorenko, G.; Oleksenko, L.; Maksymovych, N.; Skolyar, G.; Ripko, O. Semiconductor Gas Sensors Based on Pd/SnO$_2$ Nanomaterials for Methane Detection in Air. *Nanoscale Res. Lett.* **2017**, *12*, 329. [CrossRef] [PubMed]

80. Xue, D.; Wang, J.; Wang, Y.; Sun, G.; Cao, J.; Bala, H.; Zhang, Z. Enhanced Methane Sensing Properties of WO3 Nanosheets with Dominant Exposed (200) Facet via Loading of SnO$_2$ Nanoparticles. *Nanomaterials* **2019**, *9*, 351. [CrossRef] [PubMed]

81. Karaduman, I.; Güngör, A.A.; Nadaroğlu, H.; Altundaş, A.; Acar, S. Green synthesis of γ-Fe$_2$O$_3$ nanoparticles for methane gas sensing. *J. Mater. Sci. Mater. Electron.* **2017**, *28*, 16094–16105. [CrossRef]

82. Liang, J.; Liu, J.; Li, W.; Hu, M. Preparation and room temperature methane sensing properties of platinum-decorated vanadium oxide films. *Mater. Res. Bull.* **2016**, *84*, 332–339. [CrossRef]

83. Liang, J.; Li, W.; Liu, J.; Hu, M. Room temperature CH$_4$ sensing properties of Au decorated VO2 nanosheets. *Mater. Lett.* **2016**, *184*, 92–95. [CrossRef]

84. Basu, R.; Reshma, P.; Prasad, A.K.; Dhara, S. Near room temperature CH$_4$ sensing and role of oxidation states for phase pure Wadsley VnO2n+1 nanostructures. *Mater. Chem. Phys.* **2020**, *248*, 122901. [CrossRef]

85. Hu, J.; Gao, F.; Zhao, Z.; Sang, S.; Li, P.; Zhang, W.; Zhou, X.; Chen, Y. Synthesis and characterization of Cobalt-doped ZnO microstructures for methane gas sensing. *Appl. Surf. Sci.* **2016**, *363*, 181–188. [CrossRef]

86. Zhang, S.; Li, Y.; Sun, G.; Zhang, B.; Wang, Y.; Cao, J.; Zhang, Z. Synthesis of NiO-decorated ZnO porous nanosheets with improved CH$_4$ sensing performance. *Appl. Surf. Sci.* **2019**, *497*, 143811. [CrossRef]

87. Tshabalala, Z.; Shingange, K.; Dhonge, B.; Ntwaeaborwa, O.; Mhlongo, G.; Motaung, D. Fabrication of ultra-high sensitive and selective CH$_4$ room temperature gas sensing of TiO$_2$ nanorods: Detailed study on the annealing temperature. *Sens. Actuators B Chem.* **2016**, *238*, 402–419. [CrossRef]

88. Dhivya, P.; Prasad, A.K.; Sridharan, M.; Dhivya, P.; Prasad, A.K.; Sridharan, M. Nanostructured perovskite CdTiO$_3$ films for methane sensing. *Sens. Actuators B Chem.* **2016**, *222*, 987–993. [CrossRef]

89. Li, W.; Liang, J.; Liu, J.; Zhou, L.; Yang, R.; Hu, M. Synthesis and room temperature CH$_4$ gas sensing properties of vanadium dioxide nanorods. *Mater. Lett.* **2016**, *173*, 199–202. [CrossRef]

90. Mounasamy, V.; Mani, G.K.; Ponnusamy, D.; Tsuchiya, K.; Reshma, P.; Prasad, A.K.; Madanagurusamy, S. Investigation on CH$_4$ sensing characteristics of hierarchical V$_2$O$_5$ nanoflowers operated at relatively low temperature using chemiresistive approach. *Anal. Chim. Acta* **2020**, *1106*, 148–160. [CrossRef]

91. Abruzzi, R.C.; Pires, M.J.R.; DeDavid, B.A.; Galli, C.F. Application of SnO$_2$ Nanoparticles and Zeolites in Coal Mine Methane Sensors. *Mater. Res.* **2019**, *22*. [CrossRef]

92. Sedghi, S.M.; Mortazavi, Y.; Khodadadi, A.A. Low temperature CO and CH$_4$ dual selective gas sensor using SnO$_2$ quantum dots prepared by sonochemical method. *Sens. Actuators B Chem.* **2010**, *145*, 7–12. [CrossRef]

93. Yang, L.; Wang, Z.; Zhou, X.; Wu, X.; Han, N.; Chen, Y. Synthesis of Pd-loaded mesoporous SnO$_2$ hollow spheres for highly sensitive and stable methane gas sensors. *RSC Adv.* **2018**, *8*, 24268–24275. [CrossRef]

94. Zhang, S.; Li, Y.; Sun, G.; Zhang, B.; Wang, Y.; Cao, J.; Zhang, Z. Enhanced methane sensing properties of porous NiO nanosheets by decorating with SnO$_2$. *Sens.Actuators B Chem.* **2019**, *288*, 373–382. [CrossRef]

95. Zhang, D.; Yin, N.; Xia, B. Facile fabrication of ZnO nanocrystalline-modified graphene hybrid nanocomposite toward methane gas sensing application. *J. Mater. Sci. Mater. Electron.* **2015**, *26*, 5937–5945. [CrossRef]

96. Gagaoudakis, E.; Michail, G.; Katerinopoulou, D.; Moschovis, K.; Iliopoulos, E.; Kiriakidis, G.; Binas, V.; Aperathitis, E. Transparent p-type NiO:Al thin films as room temperature hydrogen and methane gas sensors. *Mater. Sci. Semicond. Process.* **2020**, *109*, 104922. [CrossRef]

97. Basu, P.; Bhattacharyya, P.; Saha, N.; Saha, H.; Basu, S. The superior performance of the electrochemically grown ZnO thin films as methane sensor. *Sens. Actuators B Chem.* **2008**, *133*, 357–363. [CrossRef]

98. Chen, T.-P.; Chang, S.-P.; Hung, F.-Y.; Chang, S.-J.; Hu, Z.-S.; Chen, K.-J. Simple Fabrication Process for 2D ZnO Nanowalls and Their Potential Application as a Methane Sensor. *Sensors* **2013**, *13*, 3941–3950. [CrossRef] [PubMed]

99. Aghagoli, Z.; Ardyanian, M. Synthesis and study of the structure, magnetic, optical and methane gas sensing properties of cobalt doped zinc oxide microstructures. *J. Mater. Sci. Mater. Electron.* **2018**, *29*, 7130–7141. [CrossRef]

100. Liu, H.; Peng, T.; Sun, H.; Xie, R.; Ma, G. Room temperature methane sensing properties of α-Fe2−xCuxO3 nanoparticles. *RSC Adv.* **2017**, *7*, 11414–11419. [CrossRef]

101. Deb, B.; Desai, S.; Sumanasekera, G.U.; Sunkara, M.K. Gas sensing behaviour of mat-like networked tungsten oxide nanowire thin films. *Nanotechnology* **2007**, *18*. [CrossRef]

102. Kanazawa, E.; Kugishima, M.; Shimanoe, K.; Kanmura, Y.; Teraoka, Y.; Miura, N.; Yamazoe, N. Mixed-potential type N$_2$O sensor using stabilized zirconia- and SnO$_2$-based sensing electrode. *Sens. Actuators B Chem.* **2001**, *75*, 121–124. [CrossRef]

103. Rout, C.; Ganesh, K.; Govindaraj, A.; Rao, C. Sensors for the nitrogen oxides, NO$_2$, NO and N$_2$O, based on In$_2$O$_3$ and WO3 nanowires. *Appl. Phys. A* **2006**, *85*, 241–246. [CrossRef]

104. Lančok, J.; Santoni, A.; Penza, M.; Loreti, S.; Menicucci, I.; Minarini, C.; Jelinek, M. Tin oxide thin films prepared by laser-assisted metal–organic CVD: Structural and gas sensing properties. *Surf. Coat. Technol.* **2005**, *200*, 1057–1060. [CrossRef]

105. Hitachi Energy. Gas-Insulated Switchgear (GIS). Available online: Https://Www.Hitachienergy.Com/It/It/Offering/Product-and-System/High-Voltage-Switchgear-and-Breakers/Gas-Insulated-Switchgear (accessed on 5 December 2021).

106. Purnomoadi, A.; Mor, A.R.; Smit, J. Spacer flashover in Gas Insulated Switchgear (GIS) with humid SF6 under different electrical stresses. *Int. J. Electr. Power Energy Syst.* **2019**, *116*, 105559. [CrossRef]

107. Purohit, P.; Höglund-Isaksson, L. Global emissions of fluorinated greenhouse gases 2005–2050 with abatement potentials and costs. *Atmos. Chem. Phys.* **2017**, *17*, 2795–2816. [CrossRef]

108. Liu, H.; Zhou, Q.; Zhang, Q.; Hong, C.; Xu, L.; Jin, L.; Chen, W. Synthesis, Characterization and Enhanced Sensing Properties of a NiO/ZnO p–n Junctions Sensor for the SF6 Decomposition Byproducts SO$_2$, SO$_2$F$_2$, and SOF2. *Sensors* **2017**, *17*, 913. [CrossRef]

109. Ramgir, N.S.; Sharma, P.K.; Datta, N.; Kaur, M.; Debnath, A.; Aswal, D.; Gupta, S. Room temperature H$_2$S sensor based on Au modified ZnO nanowires. *Sens. Actuators B Chem.* **2013**, *186*, 718–726. [CrossRef]

110. Zeng, Z.; Wang, K.; Zhang, Z.; Chen, J.; Zhou, W. The detection of H$_2$S at room temperature by using individual indium oxide nanowire transistors. *Nanotechnology* **2008**, *20*, 045503. [CrossRef]

111. Kaur, M.; Jain, N.; Sharma, K.; Bhattacharya, S.; Roy, M.; Tyagi, A.; Gupta, S.; Yakhmi, J.V. Room-temperature H$_2$S gas sensing at ppb level by single crystal In$_2$O$_3$ whiskers. *Sens. Actuators B Chem* **2008**, *133*, 456–461. [CrossRef]

112. Steinhauer, S.; Brunet, E.; Maier, T.; Mutinati, G.; Köck, A. Suspended CuO nanowires for ppb level H$_2$S sensing in dry and humid atmosphere. *Sens. Actuators B Chem.* **2013**, *186*, 550–556. [CrossRef]

113. Peng, S.; Wu, G.; Song, W.; Wang, Q. Application of Flower-Like ZnO Nanorods Gas Sensor Detecting Decomposition Products. *J. Nanomater.* **2013**, *2013*, 1–7. [CrossRef]

114. Zhang, X.; Zhang, J.; Jia, Y.; Xiao, P.; Tang, J. TiO$_2$ Nanotube Array Sensor for Detecting the SF6 Decomposition Product SO$_2$. *Sensors* **2012**, *12*, 3302–3313. [CrossRef] [PubMed]

115. Park, S.; Park, S.; Jung, J.; Hong, T.; Lee, S.; Kim, H.W.; Lee, C. H$_2$S gas sensing properties of CuO-functionalized WO3 nanowires. *Ceram. Int.* **2014**, *40*, 11051–11056. [CrossRef]

116. Zhang, X.; Yu, L.; Tie, J.; Dong, X. Gas Sensitivity and Sensing Mechanism Studies on Au-Doped TiO$_2$ Nanotube Arrays for Detecting SF6 Decomposed Components. *Sensors* **2014**, *14*, 19517–19532. [CrossRef]

117. Li, L.; Din, S.U.; Haq, M.U.; Tang, N.; Zhang, M.; Rahman, N.; Zhu, L. Room temperature monitoring of SF6 decomposition byproduct SO$_2$F$_2$ based on TiO$_2$/NiSO$_4$ composite nanofibers. *Nanotechnology* **2021**, *32*, 305705. [CrossRef]

118. Peng, S.; Wu, G.; Song, W. Synthesis, Characteristics and Enhanced Sulfur Dioxide Sensing Properties of Cu-Doped SnO$_2$ Microspheres. *Sens. Transducers* **2013**, *156*, 310–316.

119. Sun, G.-J.; Kheel, H.; Lee, J.K.; Choi, S.; Lee, S.; Lee, C. H$_2$S gas sensing properties of Fe$_2$O$_3$ nanoparticle-decorated NiO nanoplate sensors. *Surf. Coat. Technol.* **2016**, *307*, 1088–1095. [CrossRef]

120. Zhang, X.; Tie, J.; Zhang, J. A Pt-Doped TiO$_2$ Nanotube Arrays Sensor for Detecting SF6 Decomposition Products. *Sensors* **2013**, *13*, 14764–14776. [CrossRef] [PubMed]

121. Lu, Z.; Zhou, Q.; Wang, C.; Wei, Z.; Xu, L.; Gui, Y. Electrospun ZnO–SnO$_2$ Composite Nanofibers and Enhanced Sensing Properties to SF6 Decomposition Byproduct H$_2$S. *Front. Chem.* **2018**, *6*, 540. [CrossRef] [PubMed]

122. Wei, Z.; Zhou, Q.; Zeng, W. Hierarchical WO3–NiO microflower for high sensitivity detection of SF6 decomposition byproduct H$_2$S. *Nanotechnology* **2020**, *31*, 215701. [CrossRef] [PubMed]

123. Ahmad, R.; Majhi, S.M.; Zhang, X.; Swager, T.M.; Salama, K.N. Recent progress and perspectives of gas sensors based on vertically oriented ZnO nanomaterials. *Adv. Colloid Interface Sci.* **2019**, *270*, 1–27. [CrossRef]